Preparation and Characterization of Hydrophobic Surfaces

by

Mehdi Yavuz Yüce

A Thesis Submitted to the
Graduate School of Engineering
in Partial Fulfillment of the Requirements for
the Degree of

Master of Science
in
Materials Science and Engineering

Koc University

August 2006
Koc University

Graduate School of Sciences and Engineering

This is to certify that I have examined this copy of a master's thesis by

Mehdi Yavuz Yüce

and have found that it is complete and satisfactory in all respects,
and that any and all revisions required by the final
examining committee have been made.

Committee Members:

Adem Levent Demirel, Ph. D. (Advisor)

Havva Acar, Ph. D.

Alper Kiraz, Ph. D.

Date: 23/08/2006

ABSTRACT

Hydrophobic surfaces were prepared using two different methods. Emphasis has been on controllability and better characterization of their wetting properties, which are commonly classified under Wenzel and Cassie-Baxter regimes.

With the intention to collect and interpret experimental data more efficiently, results of a pioneering numerical study (the model by Johnson and Dettre) were extended to systems with controllable hydrophobicity. Analysis of the changes in contact angle and its hysteresis as a function of the same control parameter was shown to be an effective method in the determination of the governing wetting regime.

Polymer-nanoparticle composite films were studied as the first system. A slightly hydrophobic amorphous polymer (polystyrene) was mixed with a fairly hydrophobic nanoparticle at varying mass percentages. This system allowed the control of hydrophobicity by both chemical (composition) and physical (roughness) means. Collective analysis of contact angle and contact angle hysteresis data revealed the chemical effect to be more dominant for this system. In agreement with this conclusion, microscopy images and control experiments with a second type of nanoparticle showed that dispersion of nanoparticles in the polymer matrix was strongly related to the hydrophobicity of the surfaces.

The second method utilized self assembly property of a triblock copolymer (PCL-PDMS-PCL). Microphase separation in spin-coated films was tried to be used as a template for patterning the surface at different length scales. This patterning depended significantly on the resulting morphology and the molecular orientation, and did not enhance hydrophobicity as expected. As an alternative way, solutions were prepared in a selective solvent and casted into films, which exhibited super-hydrophobic behavior. DLS and AFM analyses indicated formation of micellar structures at the micro- and nanometer level.

ÖZET

İki farklı yöntem kullanılarak hidrofobik yüzeyler hazırlandı. Genellikle Wenzel ve Cassie-Baxter rejimleri olarak sınıflandırılan ıslanma özelliklerinin kontol edilebilirliği ve daha iyi tanımlanması üzerinde duruldu.

Deneysel verileri daha verimli olarak toplamak ve yorumlamak amacıyla konusunda önder işlemsel bir çalışma (Johnson ve Dettre'nin modeli) genişletilerek kontrol edilebilir hidrofobiklikteki yüzeylere uygulandı. Aynı kontrol parametresine bağlı olarak temas açısı ve temas açısı histerisisindeki değişimlerin incelenmesinin mevcut ıslanma rejiminin belirlenmesinde etkili bir yöntem olduğu gösterildi.

İlk sistem olarak polimer-nanoparçacık kompozit filmleri çalışıldı. Az hidrofobik amorf bir polimer (polisitiren) oldukça hidrofobik bir nanoparçacıkla değişen kütle yüzdelerinde karıştırıldı. Bu sistem hidrofobikliğin hem kimyasal (kompozitlik) hem de fiziksel (pürüzlülük) yollarla kontrolüne olanak sağladı. Temas açısı ve temas açısı histerisisi verilerinin birlikte analizi kimyasal etkinin bu sistem için daha baskın olduğunu gösterdi. Bu sonuçla uyumlu olarak, mikroskop görüntüleri ve ikici bir çeşit nanoparçacıkla yapılan kontrol deneyleri yüzey hidrofobikliğinin nanoparçacıkların polimer matris içindeki dağılmalarıyla yakından ilgili olduğunu gösterdi.

İkinci yöntemde üçlü blok bir kopolimerin (PCL-PDMS-PCL) kendiliğinden yapılanma özelliğinden yararlanıldı. Yüzeyi farklı ölçeklerde şekillendirmek amacıyla ince filmlerdeki mikrofaz ayrışımının bir kalıp olarak kullanılması denendi. Bu şekillenme morfolojiye ve moleküler yönlenmeye oldukça bağlı kaldı ve hidrofobikliği beklendiği şekilde arttırmadı. Diğer bir yol olarak bir seçici çözücüde çözeltiler hazırlanarak film şeklinde döküldü. Oluşan filmler süper-hidrofobik özellik sergiledi. Dinamik ışık saçılması ve atomik kuvvet mikroskobu analizleri mikrometre ve nanometre düzeyinde misel oluşumlarını işaret etti.

ACKNOWLEDGEMENTS

I would like to express my sincerest gratitude to Professor Demirel for his guidance throughout this study, which actually began when I was an undergraduate. I also owe him many thanks for his individual advice, friendship and coming to my rescue in many troublesome situations. As being the first M.S. student of his, I hope I will be reminisced with our fond memories rather than a few tense ones, and deem myself lucky for this. With separation imminent, I wish him a peaceful life.

I would also like to thank my committee members Professor Acar and Professor Kiraz for the time they spent during evaluating my thesis and progress. Their continued interest has been a source of motivation for me.

My sincere thanks are extended to Mr. Kurt, Professor Serpengüzel, Professor Alaca and of course to my undergraduate advisor Professor Sözer, for their generous help over the past six years at Koç University.

Last and perhaps most importantly, I thank my family for their support.

TABLE OF CONTENTS

LIST OF TABLES

LIST OF FIGURES

Figure 3.13: Linaer change of pinning force with the gravitational force for PS + Type-A (squares) and PS + Type-B (circles) nanoparticles. The data are collected from films having 10, 30 and 50 mass % nanoparticles (C_{PS} = 10mg/ml). Solid and dashed lines are fits to the data of Type-A and Type-B nanoparticles. Their slopes are 1.7 and 1.4 respectively. 42

NOMENCLATURE

AFM	Atomic force microscope.
F	Helmholtz free energy.
CAH	Contact angle hysteresis.
DLS	Dynamic light scattering.
E_d	Drop vibrational energy.
OM	Optical microscope.
OMCTS	Octamethylcyclotetrasiloxane.
r	Wenzel roughness ratio.
PCL	Polycaprolactone.
PDMS	Polydimethylsiloxane.
PS	Polystyrene.
SEM	Scanning electron microscope.
u_1	Fraction of horizontal distance between adjacent troughs at which the air cushion starts in the model rough surface.
V	Drop volume.
x_0	Period of the model sinusoidal surfaces.
z_0	Amplitude of the model sinusoidal rough surface.
α	Any tilt angle.
α_{crt}	The critical tilt angle.
θ	Water contact angle measured in real experiments.
θ_{adv}	Advancing water contact angle measured in real experiments.
θ_{int}	Intrinsic water contact contact angle on model surfaces.
θ_{rec}	Receding water contact angle measured in real experiments.
Φ	Macroscopically observable water contact angle for model surfaces.
Φ_0	Equilibrium water contact angle on model surfaces.

Φ_{adv}	Advancing water contact angle on model surfaces.
Φ_{rec}	Receding water contact angle on model surfaces.
ΔF^{adv}	Advancing energy barrier for model surfaces.
ΔF^{rec}	Receding energy barrier for model surfaces.

Chapter 1

INTRODUCTION

1.1 Overview

Wetting of solid surfaces by liquids, mainly water, is a practically important criterion that has to be taken into account in design of systems involving solid-liquid interfaces. Depending on the application type, a super wetting or a super water-repellent (hydrophobic) surface can be desirable. A thorough knowledge of the physical and chemical principles behind the wetting phenomenon is crucial in preparation of such surfaces. Needless to say that characterization method is also as important to provide insight for improvement. The present thesis work aims at developing new methods for preparing and sufficiently characterizing hydrophobic surfaces with tunable water repellency (hydrophobicity).

Chapter 1 begins with the definitions and the measurement methods of contact angle and contact angle hysteresis (hereafter CAH). Roughness and heterogeneity, the surface properties of importance in wettability studies, are discussed next along with the two pertaining theories.

Chapter 2 is an effort on the characterization site. Calculations based on a pioneering simulation [1,2] are employed to determine the effects of individually-varying roughness and composition on contact angle and CAH. Obtained computational results are compared with the experimental ones from literature.

Chapter 3 is about the experimental investigation of the hydrophobicity of polymer-nanoparticle composite surfaces, with an emphasis on controllability. It is primarily on the preparation site, but the results also serve as a manifestation of the conclusions from Chapter 2.

Chapter 4 deals with the thin films and solutions of a block copolymer as an attempt to develop other methods of preparing hydrophobic surfaces. Controllability over the length scales of surface roughness is tried to be achieved.

Finally, Chapter 5 concludes the thesis by summarizing the original contributions of this research.

1.2 Contact Angle as a Quantitative Measure of Surface Hydrophobicity

When a liquid forms an interface with a solid, the angle that appears between the liquid-air and liquid-solid interfaces is termed as the contact angle and conventionally denoted by θ. Figure 1.1 shows three cases for $\theta = 60^o$, 90^o and 120^o. When $\theta = 0^o$ the liquid is said to wet the solid. Partial wetting corresponds to $0^o < \theta < 90^o$. For $\theta > 90^o$ the solid is not wetted by the liquid. $\theta = 90^o$ is the transition between partial wetting and non-wetting cases. A solid that is not wetted by water is called hydrophobic (water contact angle > 90^o). As θ increases, the area of the liquid-solid interface shrinks and the interaction between the drop and the solid surface weakens. This can eventually cause the drop roll off or slide down the surface when a small force is applied. As a subclass of hydrophobic surfaces, surfaces on which water drops can easily move and have contact angles > 150^o are commonly called superhydrophobic.

Contact angle is quantitatively related to surface and interfacial energies by the Young equation,

$$\cos\theta = (\gamma_S - \gamma_{LS})/\gamma_L \tag{1.1}$$

where γ_L and γ_S are the liquid and the solid surface energies, and γ_{LS} is the liquid-solid interfacial energy. Although the equation is called Young equation, Young himself has never written such an equation; he has only expressed it qualitatively in words [3]. After much debate on the derivation and validity of the Young equation in the form of eq. (1.1), a thermodynamic proof based on the minimization of the free energy was given by Johnson [4]. It is now well understood that the contact angle obtained from Young equation corresponds to the thermodynamic equilibrium state, as long as the solid surface is perfectly homogenous and flat. In addition to homogeneity and flatness, the liquid

should not penetrate into the solid and no reactions should occur between the two as well. These conditions are violated to some extent in all real systems, and care must be taken in determining surface/interfacial energies from measured contact angle values. Nevertheless contact angle measurement is the most direct method of putting wettability in a quantitative scale. It is yet the wettability, not the surface energies; one is usually concerned with in practical studies.

Many different techniques were used in contact angle measurements depending on experimental conditions such as sample shape and the typical range of the contact angles. The most widely used technique in hydrophobicity studies is the sessile drop method, and only this will be discussed here. Information on others can be found in a review by Kwok and Neumann [5].

The sessile drop technique involves placing a liquid drop onto the solid surface, obtaining the drop shape as a two dimensional profile, and aligning a tangent with that profile at the solid-liquid-air contact point. The angle between the tangent and the solid-liquid boundary gives the contact angle.

This procedure used to be carried with special devices called goniometers, which are mainly side microscopes with a protractor installed within their eyepiece. Today, new systems that utilize the contemporary digital technology are available. With some minor differences these systems involve four basic units: a camera, a light source, a syringe and a processor unit (which is a PC in most systems). Samples are placed on a sample holder between the camera and light source. The syringe is at the top and is used for dispensing liquid drops onto the sample. There are syringes that enable very fine control (either manual or from a computer) of the volume, as well as ordinary microsyringes. Images or movies obtained by the camera are analyzed on the computer. In some models, the sample can be tilted slowly until the sessile drop on it begins to move in the downhill direction. As with the traditional goniometer, proper illumination of the sample is critical for image analysis. Especially the baseline (where liquid drop and solid surface meet) should be clearly detectable. There has to be a bright and homogenous background behind the drop to form sufficient contrast.

1.3 Effects of Roughness and Composition on Wettability

Experiments have shown that eq. (1.1), Young equation, holds only when the solid surface is flat and homogeneous. Contact angles on rough-homogeneous and flat-heterogeneous surfaces are related to those ideal ones obtained from Young equation through Wenzel [6] and Cassie-Baxter [7] relations.

Wenzel proposed the relation between contact angles on smooth and rough surfaces as

$$\cos\theta = r(\gamma_S - \gamma_{LS})/\gamma_L \tag{1.2}$$

where r is the ratio of the actual area to the projected area. This ratio can never be less than 1, indicating that a rough non-wetting surface will be more hydrophobic than the smooth one. In other words hydrophobicity will be enhanced by roughness. When r = 1, eq. (1.2) reduces to Young equation. Although eq. (1.2) successfully predicts the experimentally measured contact angles up to moderate roughness ratios, it starts to fail for rather rough surfaces, on which the liquid cannot penetrate the asperities and an air cushion forms underneath.

Cassie and Baxter extended Wenzel's analysis to such surfaces by considering them as a two-component flat surface with one of the components being air. They first suggested an averaging in cosθ values weighted by surface fractions

$$\cos\theta_{apparent} = f_1\cos\theta_1 + f_2\cos\theta_2 \tag{1.3}$$

for the apparent contact angle of a two-component smooth surface, and then replaced one of the components by air ending up with

$$\cos\theta_{apparent} = f_{solid}\cos\theta_{smooth} - f_{air} \tag{1.4}$$

Thus, the analysis of Cassie and Baxter explains the deviations from Young equation for the cases of smooth-heterogeneous and fairly rough-homogeneous surfaces.

Roughness and composition not only alter the equilibrium contact angle value, but also cause a hysteresis in its measurement (CAH). In this chapter only the measurement techniques of CAH are described. An extensive discussion on the origins of it will follow in Chapter 2. All methods for determining CAH rely on putting the system into motion and measuring the two extreme contact angles that develop as the liquid-solid contact area

spreads or shrinks. The corresponding contact angles are called advancing (θ_{adv}) and receding contact angles (θ_{rec}) respectively, and their difference is defined as the CAH. Since the drop is put into motion, the method is also termed as dynamic contact angle measurement. For similar reasons equilibrium contact angle measurements are also named as static contact angle measurements. Unlike the sessile drop method, there is no commonly accepted technique in determining CAH. Figure 1.2 depicts some of the techniques used in forming the advancing and receding configurations. After placing the drop with a syringe, its volume can be changed by adding or withdrawing liquid through the syringe until the three phase boundary moves over the solid surface giving advancing and receding contact angles (Figure 1.2.a and b). Another technique is to drag the drop over the surface with the help of an immersed syringe (Figure 1.2.c). Finally the surface can gradually be tilted after having delivered the drop onto it. Advancing and receding angles develop at the downhill and uphill directions as the drop starts moving (Figure 1.2.d).

The pinning force that resists gravity in the tilted plate case of Figure 1.2.d has been shown to be related to the CAH [8]. At the onset of the motion, the force balance can be written in the form

$$mg\sin\alpha = w\gamma_L(\cos\theta_{rec} - \cos\theta_{adv}) \qquad (1.5)$$

where m is the drop mass, g is the gravitational acceleration, α is the critical tilt angle at which the drop starts moving downhill, w is the drop base width along the motion direction (base diameter if the drop is axisymmetric), and γ_L is the surface energy of the liquid.

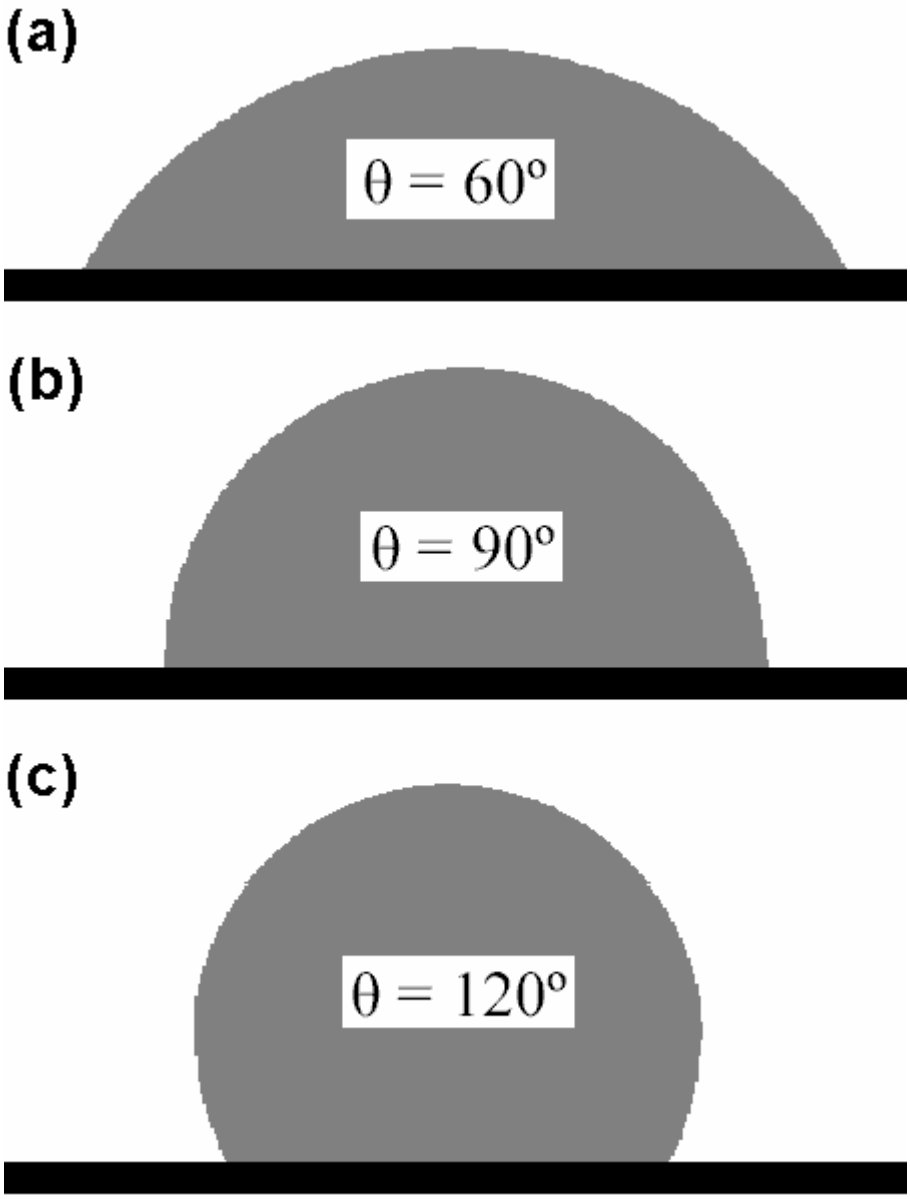

Figure 1.1: Shape of a liquid drop on a solid surface for (a) θ = 60º, (b) θ = 90º, and (c) θ = 120º. Drawn to scale with the drop volume same in all cases.

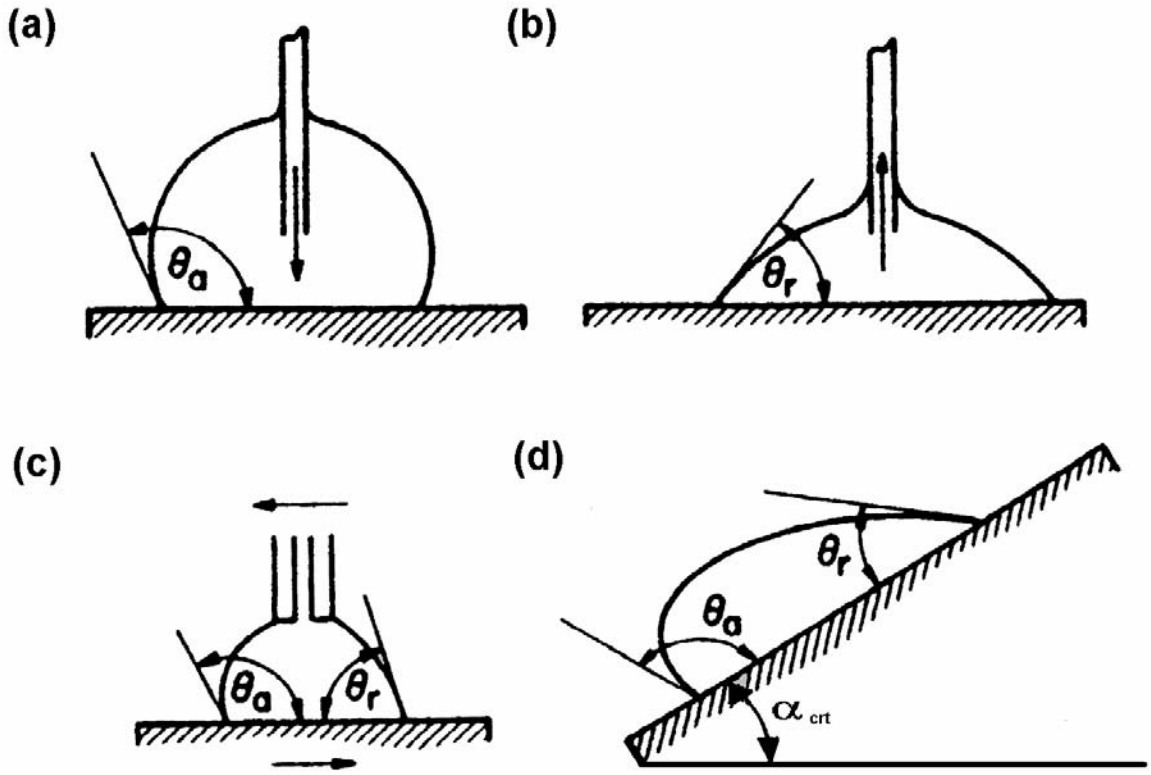

Figure 1.2: Techniques used in forming the advancing and receding contact angles.

Chapter 2

CONTRIBUTIONS OF ROUGHNESS AND COMPOSITION TO CONTACT ANGLE AND CONTACT ANGLE HYSTERESIS

2.1 Introduction

A liquid drop of constant volume, when placed on a solid surface, can take infinitely many possible configurations by adjusting its base width and contact angle. Among these possible configurations, the one with the minimum thermodynamic energy is the most probable and called the equilibrium state. The contact angle at the equilibrium state is termed as the equilibrium contact angle and is given by eq. (1.1) or equivalently eq. (1.2) with r = 1 for flat homogeneous surfaces, by eq. (1.2) with r>1 for homogeneous surfaces of moderate roughness, by eq. (1.3) for flat heterogeneous surfaces, and by eq. (1.4) for extremely rough homogeneous surfaces with its protrusions bridged by the liquid. Thermodynamic energy of a system composed of a sessile drop resting on a solid surface depends on drop volume, interfacial energies of the solid-liquid, solid-air and liquid-air interfaces, and roughness and chemical heterogeneity of the solid surface. The latter two cause energy of such a system to have local minima (metastable equilibrium states) besides its global minimum. Drops on real surfaces (i.e. rough and/or heterogeneous) will most of the time be trapped within one of these metastable states and exhibit contact angles different from their equilibrium values. This phenomenon constitutes the physics behind CAH, and has great importance for wettability studies.

As given by eq. (1.5), CAH and drop mobility are inversely proportional. Water sheds off low-CAH surfaces very easily, making these surfaces attractive for certain applications. The most conspicuous one is the drag reduction in microchannels. Experiments have shown that the famous no-slip boundary condition of fluid mechanics

does not hold for water flow past hydrophobic surfaces [9,10]. However the slip that occurred at the liquid-solid interface was not high enough to maintain considerable drag reduction. Slip lengths of practical importance (≈20μm) have been reported initially for low pressures [11] and more recently for pressures used in typical engineering applications [12]. Standard photolithography and wet etching techniques were used in the former study, which produced ordinary posts with height and separation of tens of micrometers. In the more recent work, needle-like structures of height 1-2μm and pitch 0.5-1μm were obtained using deep reactive ion etching. In both studies, the methods used for microchannel fabrication were not novel. The improvement in the performance (sustainable pressures) was a result of more careful effort in obtaining lower-CAH surfaces. This is a vivid example that demonstrates the usefulness of understanding the way CAH is influenced by chemical and physical factors.

The present chapter of the thesis consists of numerical analyses that focus on determining individual weights of roughness and composition on equilibrium contact angle and CAH. Section 2 summarizes the model systems used in calculations. Results are presented in Section 3. Section 4 concludes the chapter with a comparison of experimental studies in literature with the numerical results.

2.2 Description of Johnson and Dettre's Models

The two analyses by Johnson and Dettre [1,2] to be described in this section are for rough and composite surfaces respectively.

The model surface for roughness analysis consists of concentric grooves with sinusoidal profile. The surface is ideally homogeneous. The drop is located at the center of the circles defined by the grooves. Figure 2.1.a is a cross section through the origin. Noting the cylindrical symmetry, the equation of the surface can be expressed as

$$z = z_0(1 + \cos\frac{2\pi x}{x_0}) \tag{2.1}$$

where $2z_0$ is the bottom-to-top height of the grooves and x_0 is the period of the sinusoidal roughness. In calculations, Wenzel roughness (hereafter r) of the surfaces is

adjusted through the z_0/x_0 ratio. Figure 2.1.b shows 3-D views of surfaces with z_0/x_0 ratios of 0.1 (r = 1.092) and 0.4 (r = 1.952). θ_{int} is the intrinsic contact angle (the microscopic local contact angle), and Φ is the observed macroscopic contact angle. For example θ_{int} for a methyl surface will always be $\approx$110º regardless of the topography; however Φ will take values from 110º (flat surface) to 180º (rough surface with Cassie-Baxter effect) depending on the roughness.

As roughness increases the liquid starts bridging deep protrusions by entrapping an air cushion underneath. In the calculations this effect is taken into account by introducing a new parameter u_1. u_1 is the fraction of horizontal distance between adjacent troughs at which the air cushion starts. From symmetry $1-u_1$ will be the fraction at which the air cushion ends. Hence the values u_1 can take are bounded between 0.5 and 0 corresponding to complete wetting and complete bridging cases respectively. The latter bound is an asymptotic one that can never be achieved. Figure 2.2 shows three cases for u_1 = 0.5, 0.25 and 0.1.

The Helmholtz free energy, F, of the system is a function of drop volume (hereafter V), θ_{int}, Φ, r and u_1. Other parameters such as surface areas or interfacial tensions are included implicitly within V, θ_{int} and Φ. For given V, θ_{int}, and r values there will be a separate $F(\Phi)$ relation for each u_1, and each $F(\Phi)$ relation will have a Φ value that minimizes F. Among these minimizing Φ's the one with the lowest F is the equilibrium observable contact angle Φ_0, and its u_1 value indicates how much air -if any- is entrapped. As expected, Φ_0 calculated this way gives the Wenzel angle in complete wetting systems (u_1 = 0.5), and the Cassie-Baxter angle in air-entrapping systems ($u_1 \neq$ 0.5).

The constraints of constant V and constant θ_{int} limit Φ to have discrete values. The configurations corresponding to these Φ values are metastable states and there is one metastable state per each trough. The difference in Helmholtz free energy between two adjacent metastable states of the system is an important quantity termed "energy barrier". For a drop to remain in a given metastable state, the energy barrier of that state must be higher than the vibrational energy of the drop (E_d). Values of the energy barriers (ΔF)

depend on direction and location. That is, the energy barrier between n^{th} and $n+1^{st}$ troughs (ΔF^{adv} for the n^{th} trough) is not the same as that of n^{th} and $n-1^{st}$ (ΔF^{rec} for the n^{th} trough); also are the corresponding advancing and receding barriers different for any two non-adjacent troughs. In Figure 2.3 ΔF^{rec} and ΔF^{adv} values are plotted against Φ for a particular θ_{int} and r. The horizontal dashed line represents vibrational energy of the drop, E_d. The intersections of the horizontal line with the ΔF curves give the receding and advancing angles for the corresponding θ_{int}, r and E_d. ΔF versus Φ curves are the fundamental tool in calculating contact angle hysteresis.

The model two-component surface for heterogeneity analysis consists of concentric circular bands of alternating intrinsic contact angles of $\theta_{int,1}$ and $\theta_{int,2}$ (Figure 2.4). The surface is ideally smooth. The drop is located at the center of the circles defined by the bands. x_0 is the combined width of two adjacent bands. Relative ratio of the components is adjusted without changing x_0 (that is, by increasing the width of one of the bands while decreasing the other accordingly). Φ denotes the macroscopically observed contact angle.

As with the roughness case metastable states exist, and Φ can only take discrete values corresponding to these metastable states. Energy barriers are defined in the same way. Hysteresis values can again be computed using ΔF^{rec}, ΔF^{adv} versus Φ curves and the drop vibrational energy as for rough surfaces.

The models have some limitations also. The concentric grooves/bands of the model systems do not fully reflect the complexity of real surfaces, which usually have random roughness [13]. In the model system the three-phase contact line always has a circular profile, which necessitates the drop jump or retract the protrusions/bands in a single step. However in reality the roughness/heterogeneity is not in the form of grooves/bands but in the form of hills/islands. The three phase contact line can thus be distorted during motion. This results in lower energy barriers, and also lower contact angle hysteresis (for a given drop energy) for the real systems [14].

2.3 Results Based on Model Surfaces

This section investigates the effect of roughness and composition on equilibrium contact angle (Φ_0) and CAH (Φ_{adv} - Φ_{rec}).

Figure 2.5 compares the relation between $\cos\Phi_0$ and r for different intrinsic contact angles. Φ_0 values were obtained as described in the previous section: At each data point V, θ_{int} and r values were known in advance. Taking these as constants, the system's free energy, F, has been calculated for all possible Φ and u_1 combinations. Φ values were taken from 0.25° to 180° with 0.25° increments (720 different Φ values), and u_1 values were taken from 0.025 to 0.5 with 0.025 increments (20 different u_1 values). This corresponded to 720×20 = 14400 (Φ,u_1) pairs for each data point. The (Φ,u_1) pair that gave the minimum F was taken as the equilibrium configuration for that data point. Corresponding equilibrium u_1 values are also included as the right y-axis. The transition from Wenzel (complete wetting) regime to Cassie-Baxter (air-entrapping) regime with increasing roughness can be followed from these u_1 values.

In Figure 2.5.a the intrinsic contact angle, θ_{int}, is 92.5º and the system remains in the Wenzel regime even at high roughnesses. $\cos\Phi_0$ values are almost unaffected by the large increase in r. With such a system it is unlikely to attain Cassie-Baxter regime solely by increasing roughness. In Figure 2.5.b θ_{int} is 110º, and Cassie-Baxter regime is reached at r = 2.67 (Φ_0 = 154.5º). The graph continues to r = 3.23, where Φ_0 becomes 161.5º. The steep change in $\cos\Phi_0$ values up to the transition indicates strong relation between contact angles and roughness. However this relation dies out after the transition. A comparison between the two graphs reveals that roughness gains importance as θ_{int} increases. So composition and roughness are equally important in achieving high-contact-angle surfaces; both factors are necessary.

In most real systems experimentally accessible parameters alter both roughness and composition. This has been simulated in Figure 2.5.c by assigning a different θ_{int} value for each r; θ_{int} varies linearly from 92.5º (at r = 1) to 110º (at r = 3.23). Transition from Wenzel to Cassie-Baxter regime is delayed when compared to Figure 2.5.c (occurs at r = 3.04, Φ_0 = 154.5º). If the linearity is correct, this corresponds to a real case of mixing a

smooth material of θ_{int} = 92.5º with a rough material that has a contact angle of 161.5º at r = 3.23.

Another outcome of Figure 2.5 is related to the controllability of equilibrium contact angle. The range over which Φ_0 can reliably be controlled by some parameter is an important specification for hydrophobic surfaces that can be of technological use [15]. This range is only 6º (98.5º – 92.5º) for θ_{int} = 92.5º, and 44.5º (154.5º - 110º) for θ_{int} = 110º. As suggested by Figure 2.5.c, a solution to widen the controllable Φ range can be increasing roughness and θ_{int} together. The controllable Φ_0 range for Figure 2.5.c is 69º (161.5º – 92.5º), closer to the greatest possible value of 90º.

In a similar manner Figure 2.6 compares the relation between CAH (Φ_{adv} - Φ_{rec}) and r for different intrinsic contact angles. Drop vibrational energy, E_d, is 7.28×10^{-9}mJ for all graphs (with the original terminology of Johnson and Dettre, this value corresponds to an "energy barrier height" of 100μm). With increasing roughness, CAH increases in the Wenzel regime, reaches a plateau or peak, and then starts decreasing in the Cassie-Baxter regime [16]. This behavior of the CAH can be used to follow the transition between two regimes. In Figure 2.6.a θ_{int} is 92.5º and CAH keeps increasing without reaching a plateau or peak. This indicates that the system remains in the Wenzel regime. In Figure 2.6.b θ_{int} is 110º and CAH starts decreasing at r = 2.67. From Figure 2.5.b this is also the roughness at which the system starts forming an air cushion. Similarly in Figure 2.6.c, where θ_{int} varies linearly from 92.5º (r = 1) to 110º (r = 3.23), transition occurs at r = 3.04, again in consistence with Figure 2.5.c. Consequently the information obtained from u_1 parameter regarding the transition between wetting regimes can also be obtained from CAH. This makes CAH measurement an important tool in the characterization of hydrophobic surfaces, for there is no direct method of determining the amount of air entrapped underneath the drop.

The three graphs in Figure 2.6 look very similar up to the transition, indicating that composition has negligible effect on CAH. To test this conclusion further, CAH of a 3μL drop on a two-component smooth surface with $\theta_{int,1}$ = 110º and $\theta_{int,2}$ = 90º is plotted against composition with the same E_d of 7.28×10^{-9}mJ (Figure 2.7). As can be clearly

seen, CAH does not vary much with composition. The highest CAH on the smooth surface is ≈20º, while that on the rough surfaces is ≈120º. Hence, unlike the case for the equilibrium contact angles, only roughness is important in CAH, and composition has practically negligible contribution.

A final note has to be mentioned regarding E_d. It was taken as a constant throughout the analyses. In fact it must have some dependency on the contact angle: At higher contact angles the drop has less connection with the surface and vibrates more.

2.4 Experimental Studies from Literature

Experimental studies of the effect of surface roughness and heterogeneity on CAH have been reported by many investigators [17-20].

In the work of Ramos and Charlaix [17] swift heavy ion irradiation was used to form nanometer scale roughness (defects) on atomically smooth single crystalline $LiNbO_3$ substrates, which were then coated with OTS molecules to achieve hydrophobicity. The change of CAH of water on these surfaces was determined as a function of irradiation fluence, a parameter proportional to roughness (Figure 2.8). Formation of nanobubbles at the water-OTS interface has been suggested as an explanation to the fall of CAH after reaching its peak value. Analyses of the previous section clearly identify this as a transition from Wenzel to Cassie-Baxter regime. Hence air entrapping can occur even at nanometer scale provided that the roughness aspect ratio (in this case defect density) is high enough and the surface energy is low enough.

Semal et al. [18] investigated wetting behavior of smooth heterogeneous surfaces. They grafted mixed end-methylated and end-hydroxylated alkanethiol molecules of the same length (to avoid roughness) onto gold substrates. Water CAH was measured as a function of composition similar to graph of Figure 2.7 (Figure 2.9). The heterogeneity generated in this study was one of the most contrasting cases (OH versus CH_3 groups). However the resulting CAH values were only ≈10°, significantly less than those of Figure 2.8. This is again in agreement with the conclusion of negligible composition effect on CAH as compared to roughness effect.

The works of Murase et al. with polymeric materials [19] and of Pilotek and Schmidt with sol-gel processing [20] also report similar results, where CAH hysteresis makes a peak as a function of experimentally accessible parameters proportional to roughness.

2.5 Conclusion

Calculations of Johnson and Dettre were performed for a series of surfaces with varying roughness or heterogeneity. Although the models used in the calculations were not new, many original generalizations were arrived that have not been stated explicitly and collectively before.

Low surface energy and roughness were shown to be achieved together in order to obtain high equilibrium contact angles. They are equally important for the static contact angle. On the contrary, composition had almost negligible effect on CAH when compared to roughness. Complimentary use of static and dynamic contact angle measurements provided successful determination of the dominant wetting regime and the occurrence of a transition.

Section 2.4 showed that these results are consistent with experimental studies, suggesting that the limitations of the model system are not big of a problem. The analysis is interesting in its simplicity and success.

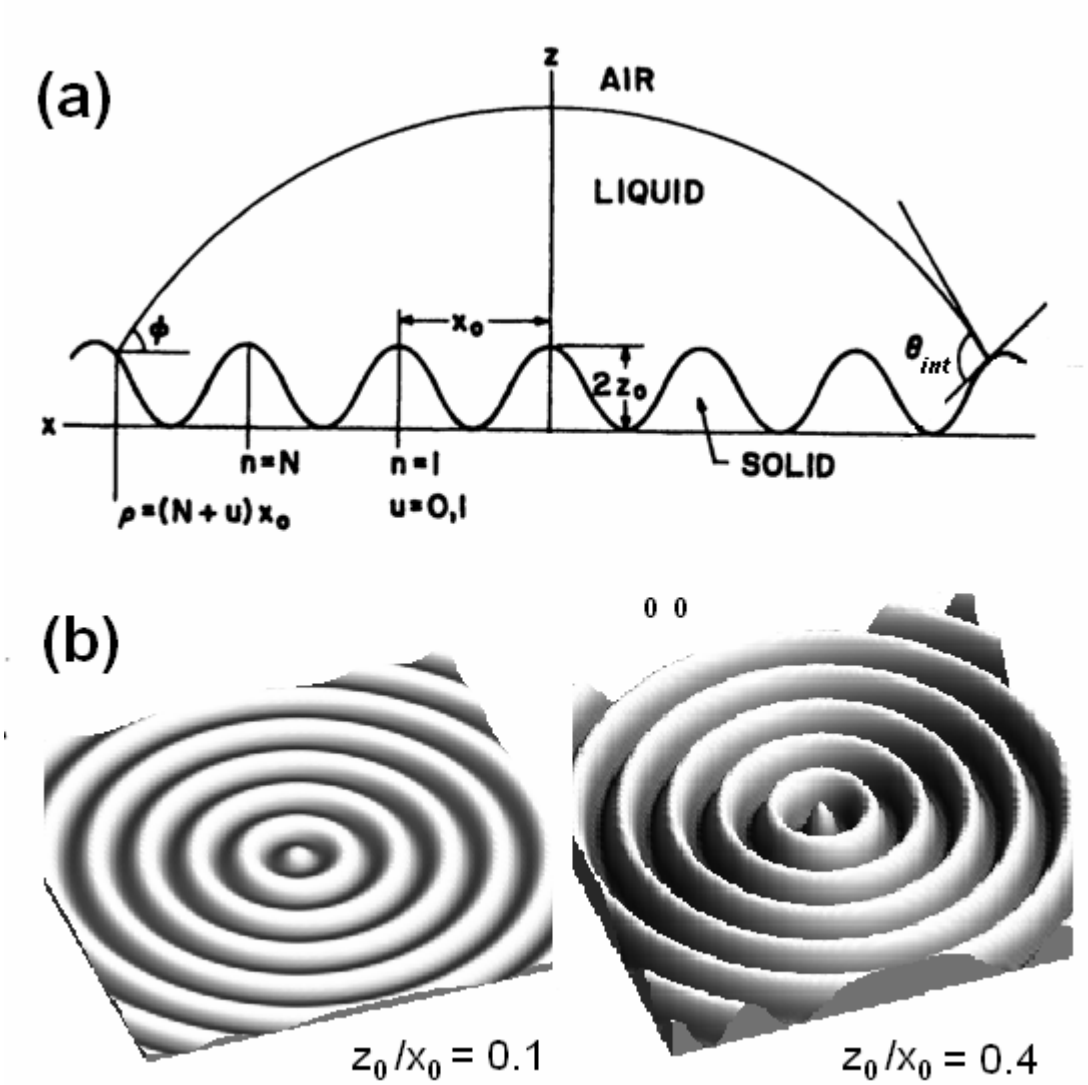

Figure 2.1: a) Illustration of a drop sitting on the model surface. Φ is the macroscopic contact angle, θ_{int} is the intrinsic contact angle, x_0 is the roughness period, z_0 is the height of the troughs, ρ is the drop radius, and u is the fraction of the distance along the x axis (radial direction) between adjacent crests. (After Ref. 1.) b) Isometric views of surfaces with z_0/x_0 ratios of 0.1 (r = 1.092) and 0.4 (r = 1.952).

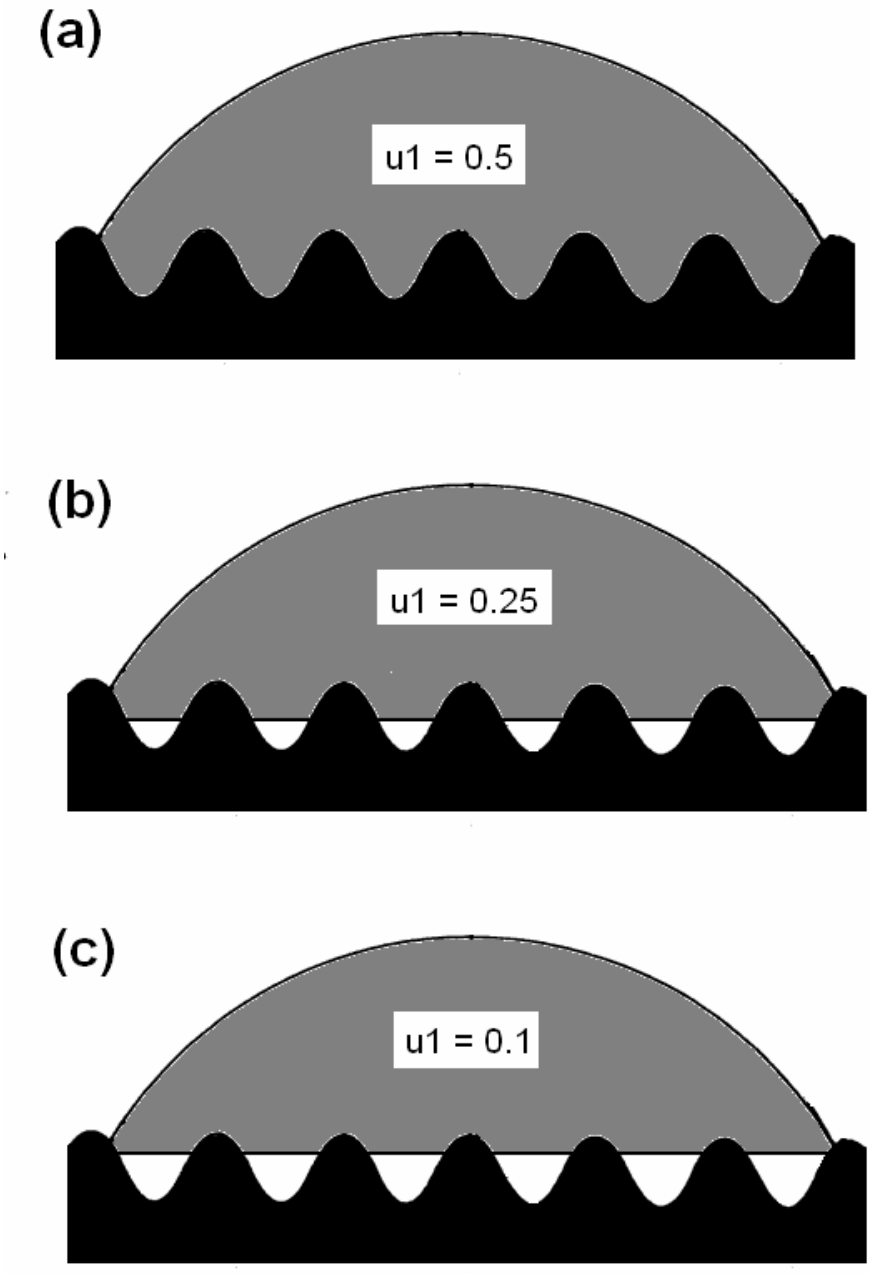

Figure 2.2: Illustrations to clarify definition of u_1 parameter: a) $u_1 = 0.5$, b) $u_1 = 0.25$, and c) $u_1 = 0.1$.

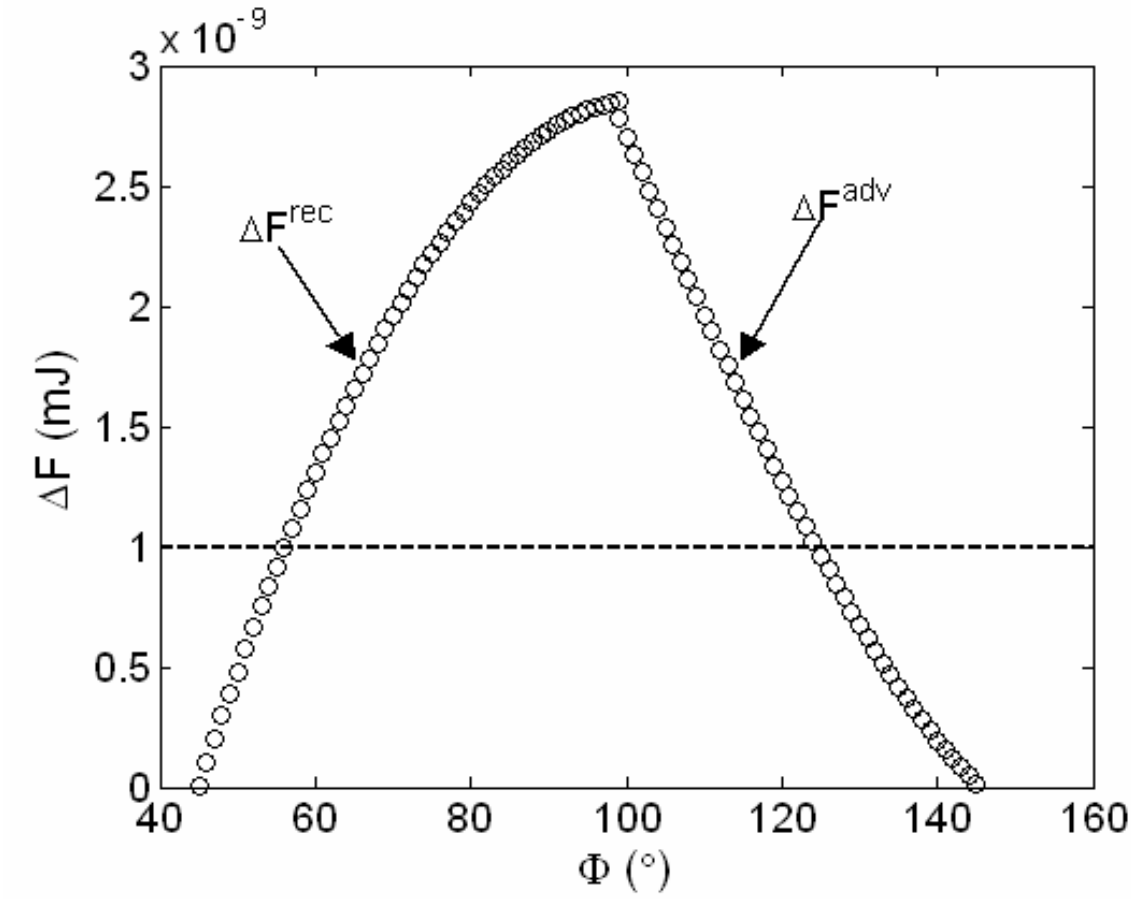

Figure 2.3: Change of ΔF^{adv} and ΔF^{rec} with Φ for V = 3μL, θ_{int} = 95º, r = 1.62 (z_0/x_0 = 0.3) and u_1 = 0.5. Vibrational energy of the drop, E_d, corresponds the dashed line (E_d = 10^{-9}mJ). Its intersections with ΔF^{rec} and ΔF^{adv} curves give the receding (56º) and advancing (124º) contact angles.

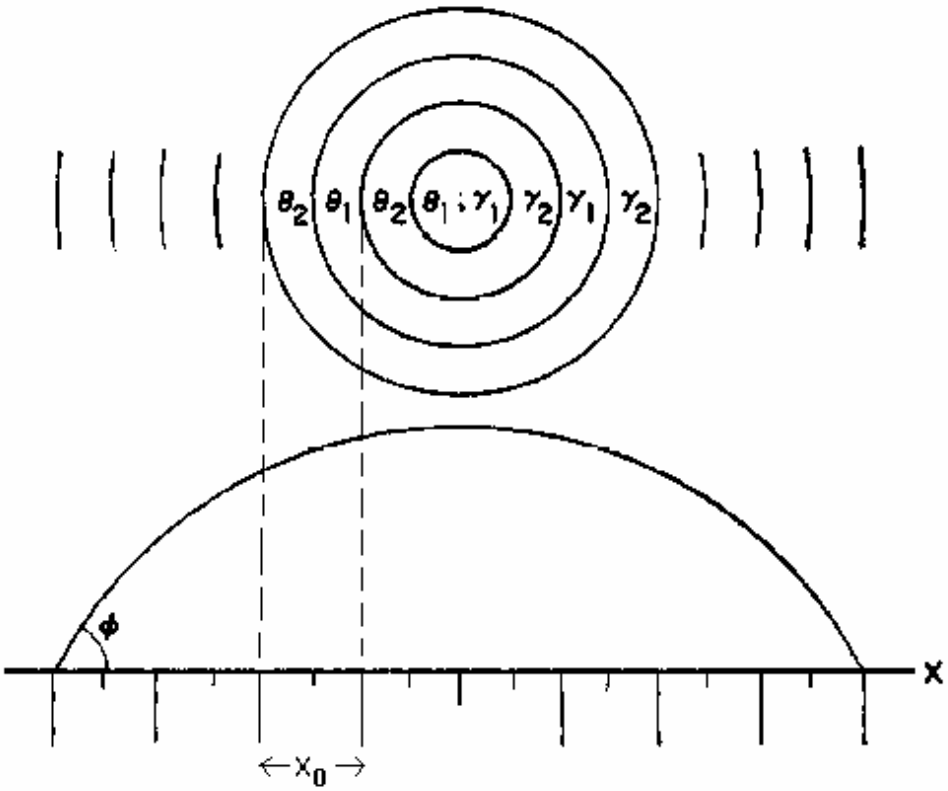

Figure 2.4: Top and side views of the two-component model surface used in heterogeneity analysis. Φ is the macroscopic contact angle, $\theta_{int,1}$ and $\theta_{int,2}$ are the intrinsic contact angles and x_0 is the heterogeneity period. (After Ref. 2.)

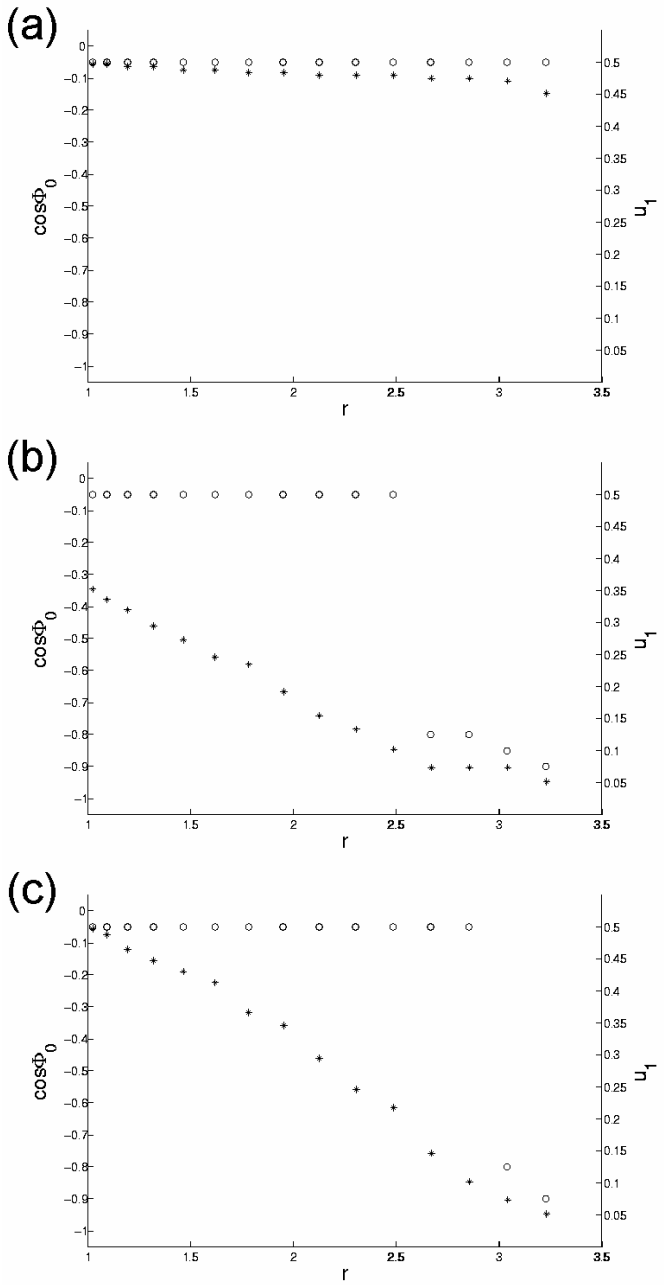

Figure 2.5: Change of $\cos\Phi_0$ of a 3 μL water drop with Wenzel roughness, r, on idealized sinusoidal surfaces with constant periodicity of $x_0 = 1\mu m$. The intrinsic contact angle, θ_{int}, is constant at 92.5º and 110º for (a) and (b), and varies linearly from 92.5º to 110º for (c). Asterixes belong to left y-axis ($\cos\Phi_0$) and open circles belong to right y-axis (u_1).

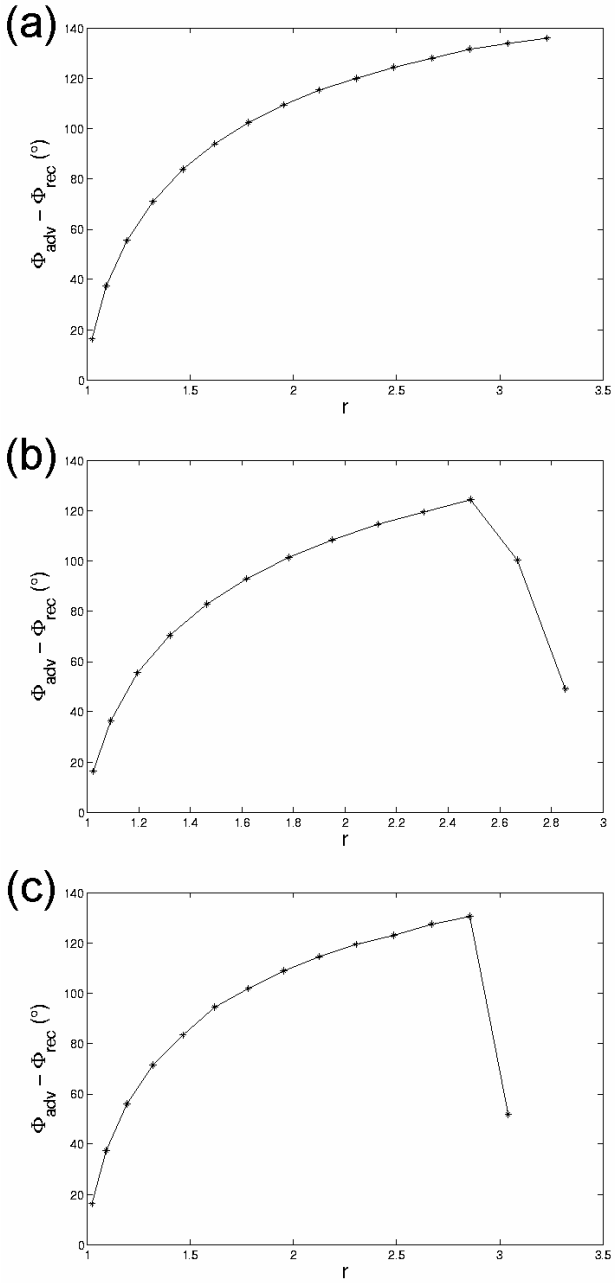

Figure 2.6: Change of CAH (Φ_{adv} - Φ_{rec}) of a 3 µL water drop with Wenzel roughness, r, on idealized sinusoidal surfaces with constant periodicity of x_0 = 1µm. The intrinsic contact angle, θ_{int}, is constant at 92.5º and 110º for (a) and (b), and varies linearly from 92.5º to 110º for (c). $E_d = 7.28\times10^{-9}$mJ for all graphs.

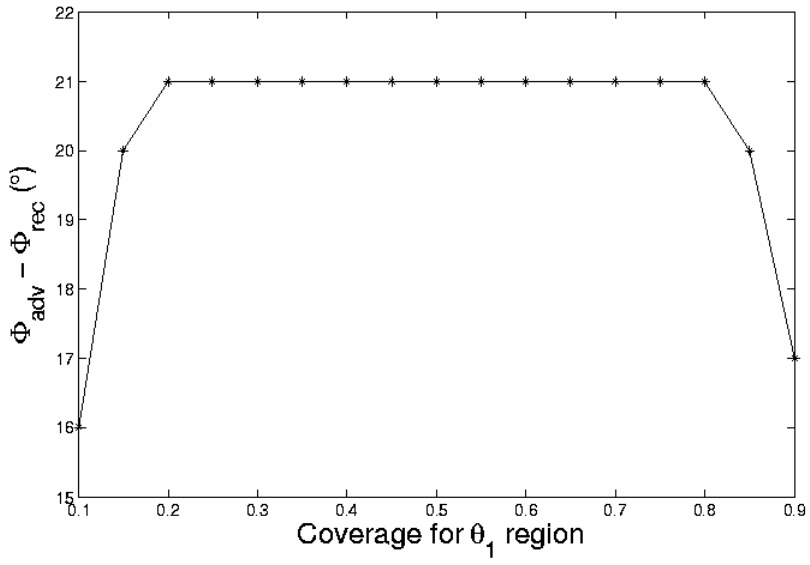

Figure 2.7: Change of CAH (Φ_{adv} - Φ_{rec}) of a 3 μL water drop with composition on an idealized two-component surface of $\theta_{int,1}$ = 110º, $\theta_{int,2}$ = 90º and x_0 = 1μm. Drop energy, $E_d = 7.28\times10^{-9}$mJ.

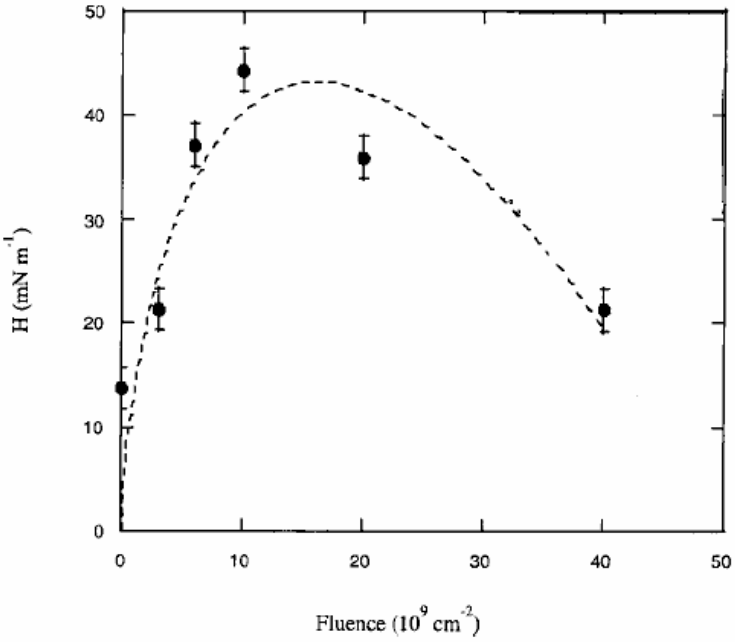

Figure 2.8: Change of CAH with irradiation fluence. (After Ref. 17.)

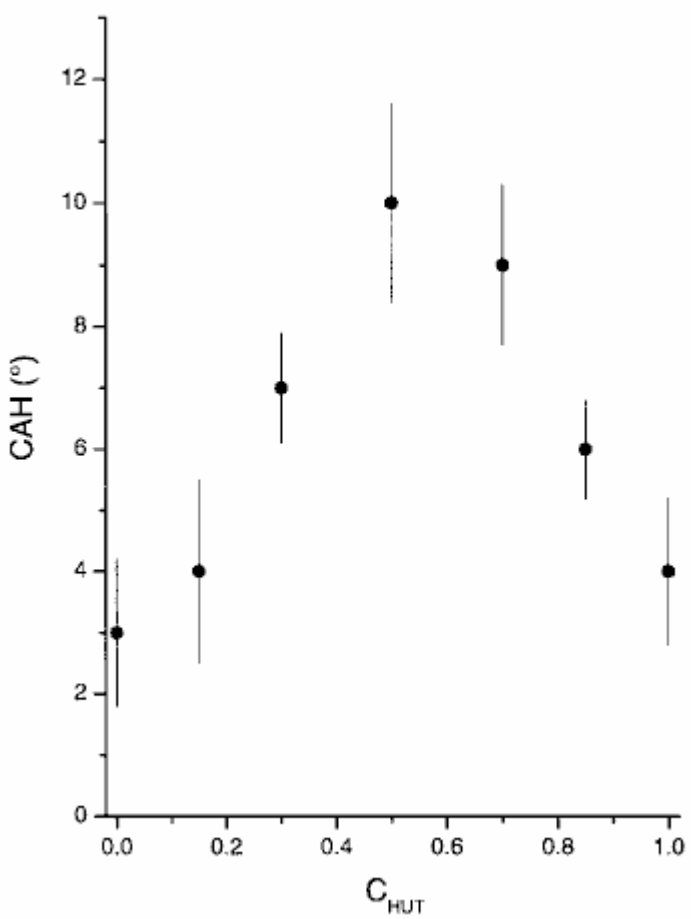

Figure 2.9: Change of CAH with the surface fraction of the hydroxyl groups (C_{HUT}). (After Ref. 6.)

Chapter 3

NANAOPARTICLE – POLYMER COMPOSITE FILMS

3.1 Introduction

Polymer-nanoparticle composites find increasing application areas, where control over mechanical, optical/electrical and surface properties is desired [21-24]. Wettability is among the most important surface properties of solids, and depends on both chemistry and physical structure of the surface.

Surfaces with variable hydrophobicity serve as model systems for understanding the mechanisms that would allow control over wettability. Besides their fundamental importance, such mechanisms can also be of practical use, provided that they can be applied for tuning the wettability of a surface gradually. Surfaces with spatially and uniformly variable wettability are commonly called gradient surfaces. When a liquid drop is placed on a gradient surface, unbalanced forces develop as a consequence of the variable wettability. These forces can cause the drop move on the surface, if their difference is greater than the force due to CAH. Such gradient surfaces can be prepared using gradual chemical adsorption [25], asymmetric irradiation of photoisomeric monolayers [26] or the chemical interactions between the surface molecules and the acid/base [27] or surface active [28] molecules suspended within the liquid drop.

When polymer-nanoparticle composites are concerned, wettability can be controlled both physically (by roughness) and chemically (by composition). In order to obtain surfaces with desired hydrophobicity, it is necessary to know how the surface roughness and composition are related to the experimentally controllable parameters. It is clear that mixing nanoparticles with a polymer will alter roughness and composition at the same time. Though this may seem as a disadvantageous situation for control purposes,

their coupled change has shown to provide a broad range of controllable contact angles in the analysis of Chapter 2. This property of composite rough surfaces can be in demand in future designs.

3.2 Experimental

Commercial silica nanoparticles, hydrophobized with surface groups of dimethylsilyl, were kindly provided by Degussa AG, Hanau, Germany. Two types were used: Type-A: Aerosil®R974, and Type-B: Aeroxide®LE1. Both types have primary particle sizes of 12 nm. Following functional modification Type-B particles were further undergone a mechanical treatment that ensured lower agglomeration as compared to Type-A particles.

Polystyrene, PS, (Fluka, MW = 65,000 g/mol, polydispersity = 1.02) was used as the polymer. Nanoparticles were mixed with PS in chloroform at varying mass percentages. PS concentration was kept constant in solutions, and the particle mass percentages were adjusted accordingly. Following 30 min. of sonication, films were prepared by spin coating the solutions onto glass substrates (hydrolytic class 1 borosilicate glass) at 2000 rpm for 1 min.

Water contact angle measurements were performed by a homemade setup consisting of a light source, a digital camera, and a sample stage in between (all on the same plane). Contact angle hysteresis measurements (CAH) were done using tilted plate method with a tilt speed of 3º/s. (Figure 3.1). For the drops that rolled off or slid down CAH is recorded as the difference between advancing and receding contact angles at the critical tilt angle at which motion started. For the drops that did not roll off or slide down (pinned to the surface), CAH is taken as the difference between advancing and receding contact angles at 90º tilt angle, where the pinning force is maximum.

Optical microscope, OM, (Leica DMLM), atomic force microscope, AFM, (NT-MDT Solver P47), and scanning electron microscope, SEM, (Zeiss FESEM) were used for determining surface topography and homogeneity of the films.

3.3 Results and Discussion

3.3.1 Homogeneity of the Composite Films

At the initial stage of this study nanoparticle-polymer solutions were prepared using toluene instead of chloroform. In the films from toluene solutions nanoparticles formed 1-5 μm large lumps and did not disperse within the polymer. This hindered their effect on surface composition, resulting in no noticeable change in the water contact angle values. Wettability remained the same after 8 hours of annealing at 100ºC (T_g of PS ≈ 95°C). Switching the solvent to chloroform improved homogeneity significantly. Figure 3.2 shows the difference between surface homogeneities of the films prepared from solutions in toluene and chloroform with comparable nanoparticle mass percentages (≈15%). The choice of solvent is mainly a trial and error process based on experience. All the samples to be discussed henceforth are prepared with chloroform.

The two nanoparticle types exhibited different miscibility with PS. Better dispersion and less agglomeration of Type-B particles can be seen in Figure 3.3. The 65μm×65μm AFM height images are from PS + nanoparticle composite films prepared with Type-A and Type-B particles at comparable mass percentages (≈20%).

3.3.2 Change of Contact Angle with Composition

Water contact angles, θ, on films of pure PS, pure Type-A particles and pure Type-B particles were measured as 93±3º, 160±3º and 140±3º respectively (Figure 3.4). Wettability of the mixed PS nanoparticle films was characterized by contact angle and CAH measurements.

Contact angles of the composite films changed from 93º to the contact angles of the nanoparticle with increasing nanoparticle mass %. Figure 3.5 shows the variation of cosθ with particle mass % in the composite films of Type-A particles prepared at three different PS concentrations (5, 10, and 20mg/ml). Two different linear regions are common for all concentrations. These linear regions connect each other with a sharp change in cosθ, which occurs at different mass percentages depending on the PS

concentration. As the PS concentration changed from 5mg/ml to 20mg/ml, the transition shifted to smaller mass % of particles.

Figure 3.6 presents CAH versus Type-A nanoparticle mass % relation for two set of films prepared from solutions having PS concentrations of 5 and 10mg/ml. Except for the 100 % nanoparticle films, water drops were pinned on the surface. For both set of films CAH increases –within the limits of experimental accuracy– uniformly with the increasing particle mass % (dotted lines are drawn to help follow this trend). As an important change, the sharp transition in the cosθ plot disappeared here.

CAH values on rough surfaces can be quantitatively predicted from the CAH on the corresponding smooth surface, using the idea of contact angle amplification proposed recently [16]. The smooth surface here is not an ideal one. It has a small but nonzero CAH, such as pure PS film. The smooth and rough CAH are related with a gain factor, which is a function of roughness and the equilibrium contact angle on the smooth surface. For the present case, the latter one can be calculated from eq. (1.3) with the particle mass percentages used as surface fractions. Roughness values are then obtained through eq. (1.2) using the experimental contact angle values as the rough ones. The gain factor can be calculated from these. Finally, assuming the CAH on pure PS (12º) to be equal to those on the smooth surfaces of other films (which are not possible to obtain experimentally), CAH on rough surfaces can be calculated for all particle mass percentages. The solid line in Figure 3.6 represents the calculated CAH values, and is in good agreement with the experimental data.

As discussed in Chapter 2 contact angle and CAH data compliment each other and their combined analysis helps identifying roughness and composition effects, especially for the systems where they cannot be controlled separately. An example of such systems are the present PS-nanoparticle composite films, where varying the nanoparticle mass % alters roughness and composition simultaneously. Thus it will be appropriate to consult results of Chapter 2 in explaining the existence of two different linear regions in the cosθ data.

The three intrinsic contact angle, θ_{int}, cases (92.5º, 110º and variable) of Figures 2.5 and 2.6 are the same as one would expect to have with PS, nanoparticle and composite films. Pure PS surface is extremely smooth with root-mean-squared roughness of ≈5nm as determined from AFM height images. Owing to this smoothness, the experimentally measured contact angle of 93±3° for PS surface has to be close to the ideal θ_{int}. θ_{int} for PS can be accepted as 92.5º. Pure nanoparticle surface is rough, and needs to be put into a smooth form to determine its θ_{int}. Recalling that the individual nanoparticles are coated with methyl groups, one can use the contact angle on a flat methyl surface as their intrinsic contact angle. Such surfaces can readily be obtained by the well-known formation of alkyltrichlorosilane monolayer on atomically smooth Si wafer. θ_{int} determined for the nanoparticle using this method is 110°. From Figure 2.5.b the experimentally measured contact angle of 160±3° for the pure nanoparticle surface corresponds to a roughness of r = 3.23. Hence, introducing nanoparticles into PS changed θ_{int} from 92.5° to 110°, and r from 1 to 3.23. The graph in Figure 2.5.c has been obtained with the same values, assuming a linear relation between θ_{int} and r. Comparing this with the experimental cosθ vs. particle mass % graph of Figure 3.5 reveals that either roughness or the intrinsic contact angle (composition) did not vary so smoothly with the particle mass %. If the sharp transition were due to roughness, one would also expect to see a corresponding discontinuity in the CAH vs. particle mass % graph (Figure 3.6), for because CAH data are as sensitive as cosθ data to roughness. However no such discontinuity exists. This suggests that the sharp change in cosθ graph is due to composition and thus not seen in the CAH graph owing to the significantly small contribution of composition to CAH when compared to that of roughness (Section 2.3).

The conclusion arrived in the previous paragraph is indeed well supported by OM, SEM and AFM data. Figure 3.7 shows OM images (reflection mode) of a 650μm×900μm area of PS + Type-A nanoparticle films prepared from solution having 10mg/ml PS concentration. Particle mass percentages are 30.6, 40.0 and 50.0 (from top to bottom), which are right on the transition as can be followed from Figure 3.5. In

Figure 3.7.a, the surface is composed of islands of nanoparticles in the continuous PS matrix, then turns into islands of flat PS regions in the continuous nanoparticle matrix in Figure 3.7.b, and finally becomes almost completely covered by nanoparticles in Figure 3.7.c.

The contrast between polymer and nanoparticle rich regions is more evident in SEM images, examples of which are shown in Figure 3.8 for the film containing 40.0 mass % Type-A nanoparticles (PS concentration in the solution is 10mg/ml). Figure 3.8.a is from a 265μm×350μm area. Existence of two regions with approximate size ~40μm is clearly seen. When compared with the size of the water drop (≈2mm) these regions are so small that their contributions to contact angle is averaged out. Figure 3.8.b is a detail of 13μm×17μm area, revealing that the darker areas correspond to nanoparticle rich regions (lower right), and the lighter areas correspond to regions where some flat PS films are seen (upper left).

In addition to OM and SEM, the samples along the transition have also been analyzed with AFM to get a quantitative measure of the roughness involved. Figure 3.9.a-c presents 5μm×5μm AFM height images of PS + Type-A nanoparticle films of 48.11, 54.40, and 69.40 particle mass percentages, which correspond to points A-C in Figure 3.5. The color bars have very close ranges, indicating that roughness has not changed much along the transition. Aggregate heights are ~150nm in Figure 3.9.a, ~150-200nm in b, and ~80-120nm in c. Root mean squared roughness values are also similar: 46nm in a, 66nm in b, and again 66nm in c.

Consequently, the aforementioned observations from microscopy techniques manifest that the sharp change in the cosθ graph is primarily a composition effect. This is in perfect agreement with the results driven based on the outcomes of Chapter 2.

Following this conclusion two control experiments were performed to gain further insight. As mentioned earlier, the sharp change in cosθ graph was dependent on the PS concentration of the solutions; shifting to smaller particle mass percentages with increasing PS concentration. However, the particle concentration at the onset of the transition was nearly constant at 4.65mg/ml. This occurs to mind a critical particle

concentration of 4.65 mg/ml, at which the composition changes significantly. As the first control experiment, solutions that involved only the Type-A nanoparticles (i.e. no PS) were prepared at varying concentrations and coated onto glass substrates. Water contact angles of the resulting films changed from that of bare substrate (60°) to 160° as the nanoparticle concentration increased (Figure 3.10). The sharp change exists also in the absence of PS, showing that it is inherent to Type-A particles. Although the jump in the contact angles did not occur at exactly 4.65mg/ml, it was quite illuminating to see the same behavior. As a result, aggregation of Type-A particles makes controlling their coverage with concentration coarser around ~5mg/ml.

Having determined the reason for the sharp change, another control experiment was carried to test if a smoother change in the contact angles of the composite films could be achieved with a better-dispersing type of particle. The same procedure as for Type-A nanoparticles was followed to prepare composite films of PS + Type-B nanoparticles at varying nanoparticle mass percentages. The resulting cosθ versus particle mass % graph shows a linear change from cos(93°) to cos(140°) (Figure 3.11). This result was independent of the PS concentration of the solutions. Substrate effect was also tested by coating onto silicon substrates, and similar results were obtained. Finally, repeating the first control experiment with Type-B particles resulted in a more gradual change of contact angle with concentration (Figure 3.12).

3.3.3 Pinning Force in Wenzel Regime

Eq. (1.5) has provided a relation between the pinning force and the critical tilt angle. Indeed, the same relation can be used at any tilt angle α in the form

$$mg\sin\alpha = w\gamma_L(\cos\theta_{downhill} - \cos\theta_{uphill}) \quad (3.1)$$

As the surface is tilted the two angles in the downhill and uphill directions ($\theta_{downhill}$ and θ_{uphill}) approach receding and advancing angles, and become equal to them at the critical tilt angle. Just like the friction force, pinning force ($w\gamma_L(\cos\theta_{downhill} - \cos\theta_{uphill})$) adjusts itself to balance an external force (in this case gravity).

The pinning forces were calculated for both PS + Type-A and PS + Type-B nanoparticle composite films at 10, 30 and 50 particle mass %. They were found to change linearly with the gravitational force. The resulting data is plotted in Figure 3.13. At all tilt angles pinning force is greater than the gravitational force. Slopes of the fitted lines are 1.7 for Type-A (solid line), and 1.4 for Type-B (dashed line) nanoparticles. For an ideal experiment this slope would be 1, as suggested by eq. (3.1). It is not clear at this point whether these slightly different slopes indicate any difference in the response of the contact angles to an external force. However the linear behavior is not expected to be observed in a similar graph obtained from systems dominated by Cassie-Baxter regime. The slope in that case must approach 1, for because the drops will eventually roll off at some tilt angle. All the composite films studied in this chapter were in Wenzel regime. Nevertheless linearity of the pinning force versus gravitational force graphs can be used as an indicator of the wetting regime for the mixed cases.

3.4 Conclusion

In this chapter wettability of hydrophobic polymer-nanoparticle composite films has been studied as a function of composition. It was shown that surface hydrophobicity can be tuned by adjusting the amount of particles in the two-component system. A discontinuity was observed in water contact angles of the composite films as they evolved from pure polymer to pure nanoparticle surface. Based on CAH measurements and results of Chapter 2, the discontinuity was shown to be a composition effect, rather than roughness. Microscopy images supported this conclusion.

When a slightly different nanoparticle of better dispersion was used, contact angles of the composite films changed smoothly between those of polymer and nanoparticle.

Wetting of the composite films with either types of nanoparticles were governed by Wenzel regime, as evidenced from CAH measurements.

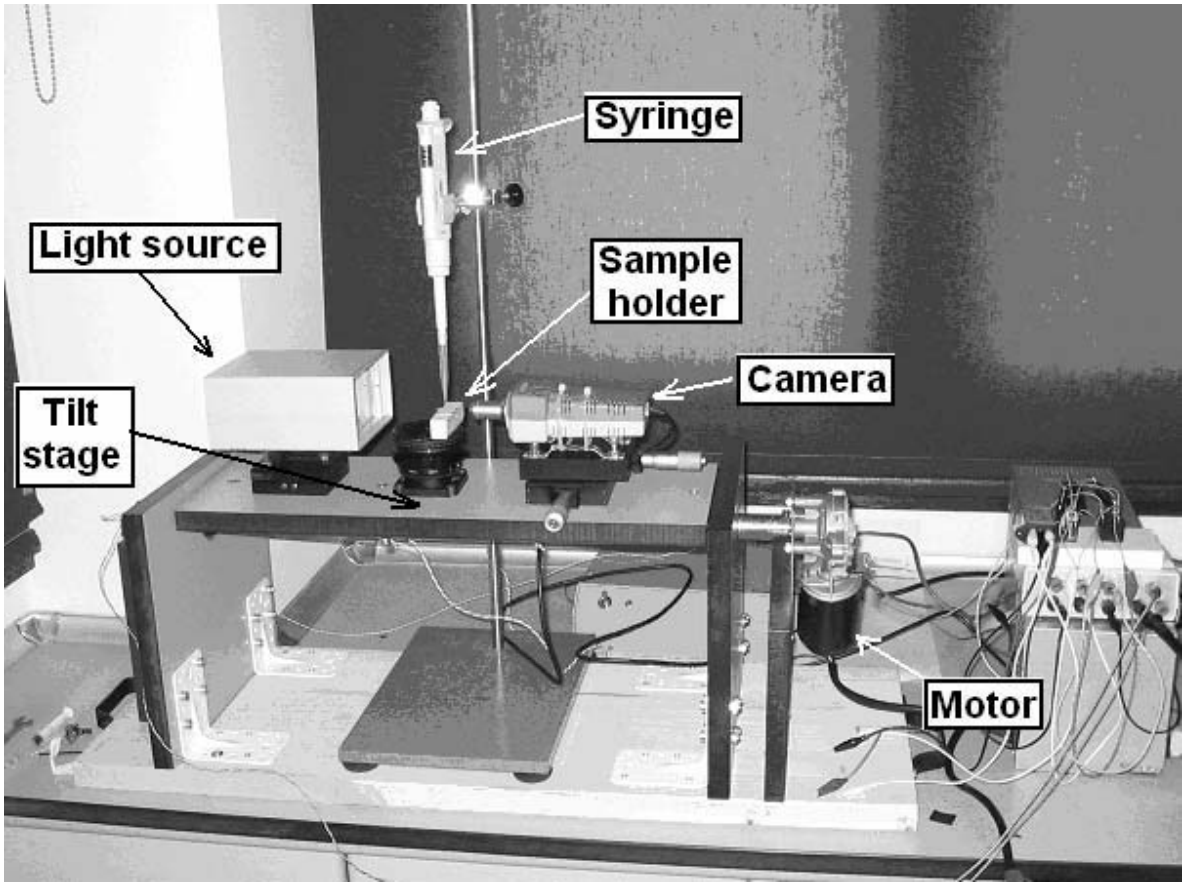

Figure 3.1: Photograph of the contact angle measurement setup with relevant components (camera, light source, sample holder, syringe, motor, tilt stage) labeled on the picture.

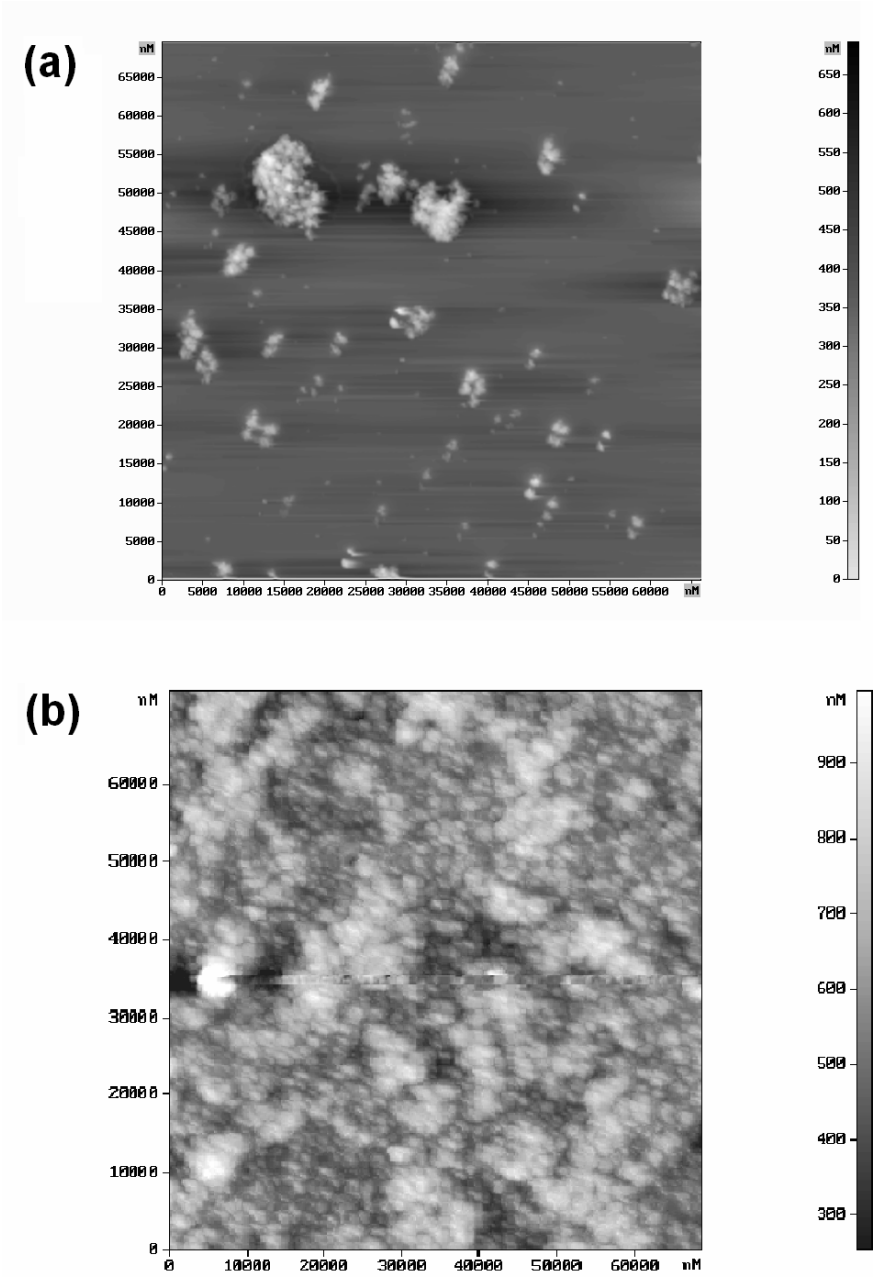

Figure 3.2: 65μm×65μm AFM height images of composite films coated from solutions prepared with (a) toluene, and (b) chloroform. Nanoparticle mass percentages are 16.43% and 13.72% respectively. Nanoparticles mix with PS much better when chloroform is used as solvent.

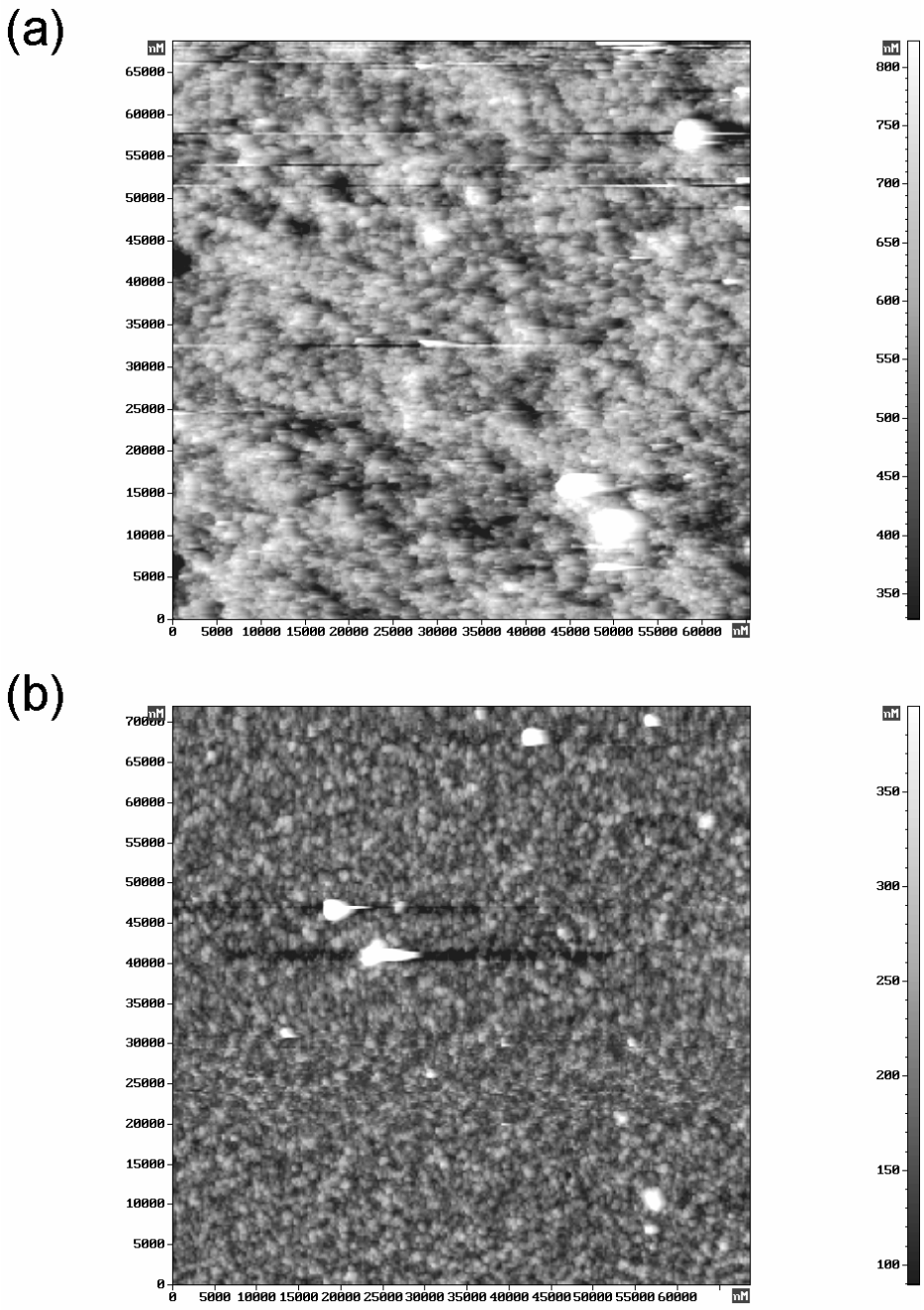

Figure 3.3: 65μm×65μm AFM height images of composite films containing (a) 18.33 mass % Type-A, and (b) 20.23 mass % Type-B nanoparticles. Better dispersion of Type-B nanoparticles can clearly be detected.

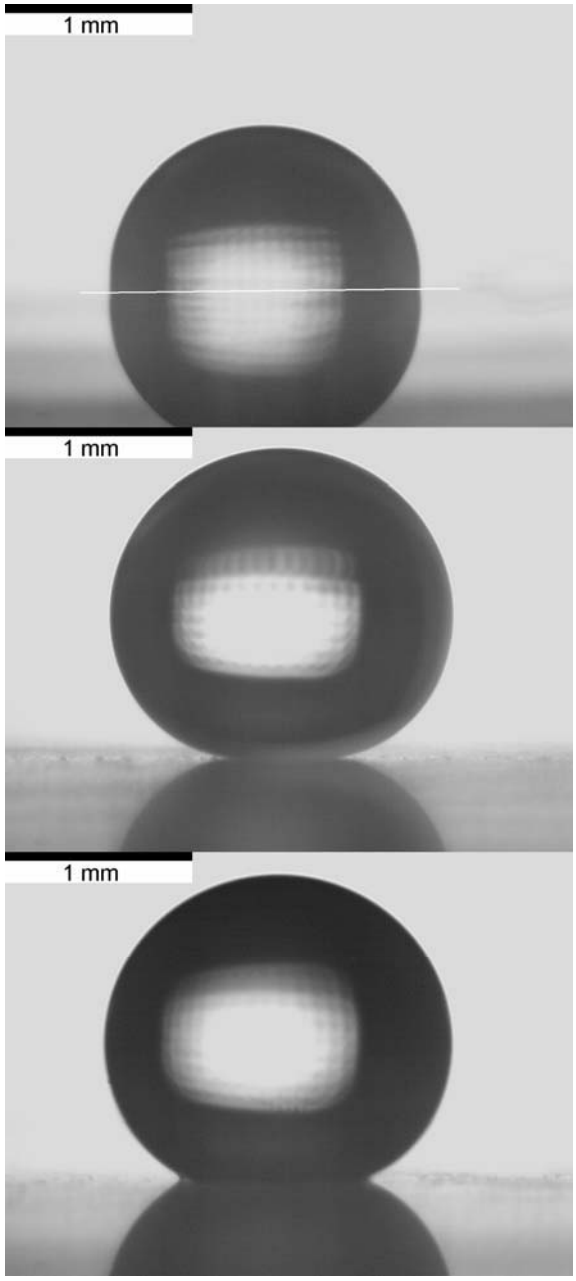

Figure 3.4: Shape of a ~3μL water drop on films of pure PS (top), pure Type-A particles (center), and pure Type-B particles (bottom). Measured contact angles are 93±3º, 160±3º and 140±3º respectively. The white line in the top image is to distinguish between the drop and its reflection on the specular PS surface.

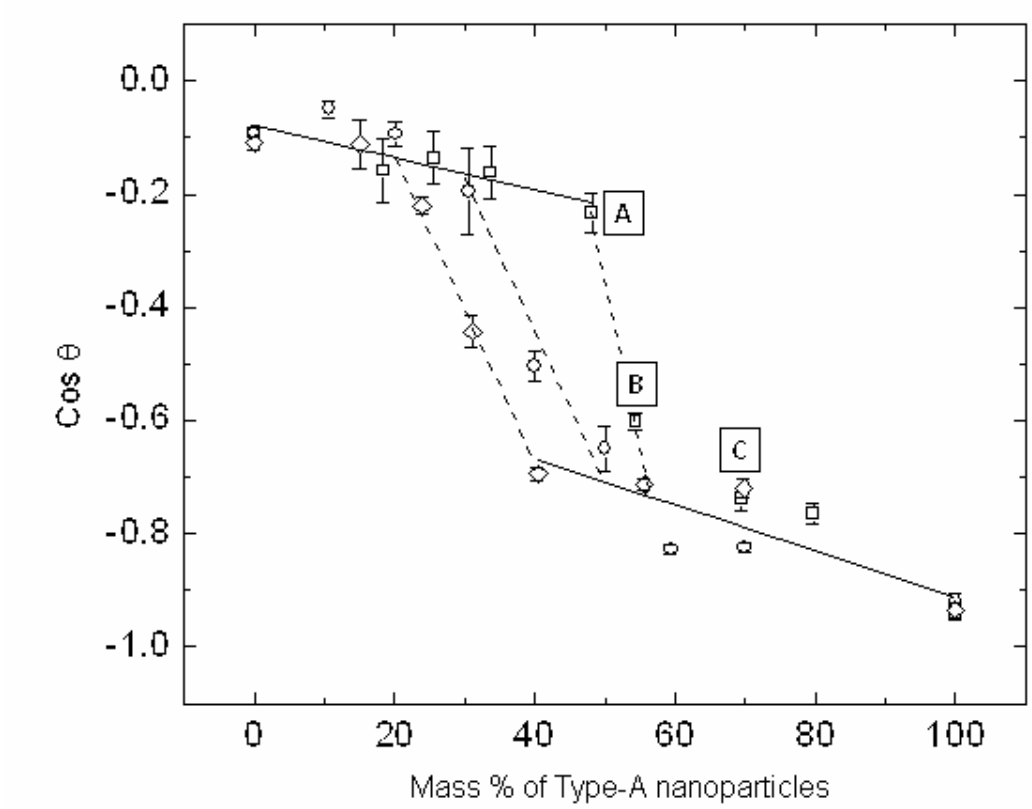

Figure 3.5: Nonlinear change of cosθ with mass % of Type-A nanoparticles. The sharp change in contact angles occurs at different mass percentages, depending on the PS concentration of the spin coated solutions. Three different sets of films were prepared from solutions having PS concentrations of 20 mg/ml (diamonds), 10 mg/ml (circles) and 5 mg/ml (squares). The solid lines are to guide the eye. Dashed lines indicate transitions.

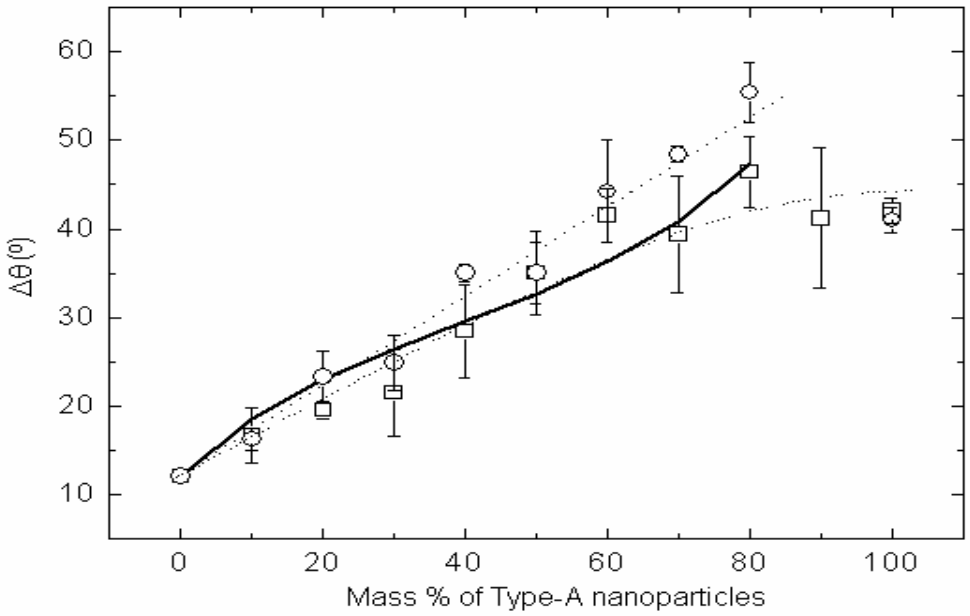

Figure 3.6: Change of CAH with mass % of Type-A nanoparticles. Two different sets of films were prepared from solutions having PS concentrations of 10 mg/ml (circles) and 5 mg/ml (squares). Dotted lines are to guide the eye. The solid line is calculated according to Ref. 16 as described in the text.

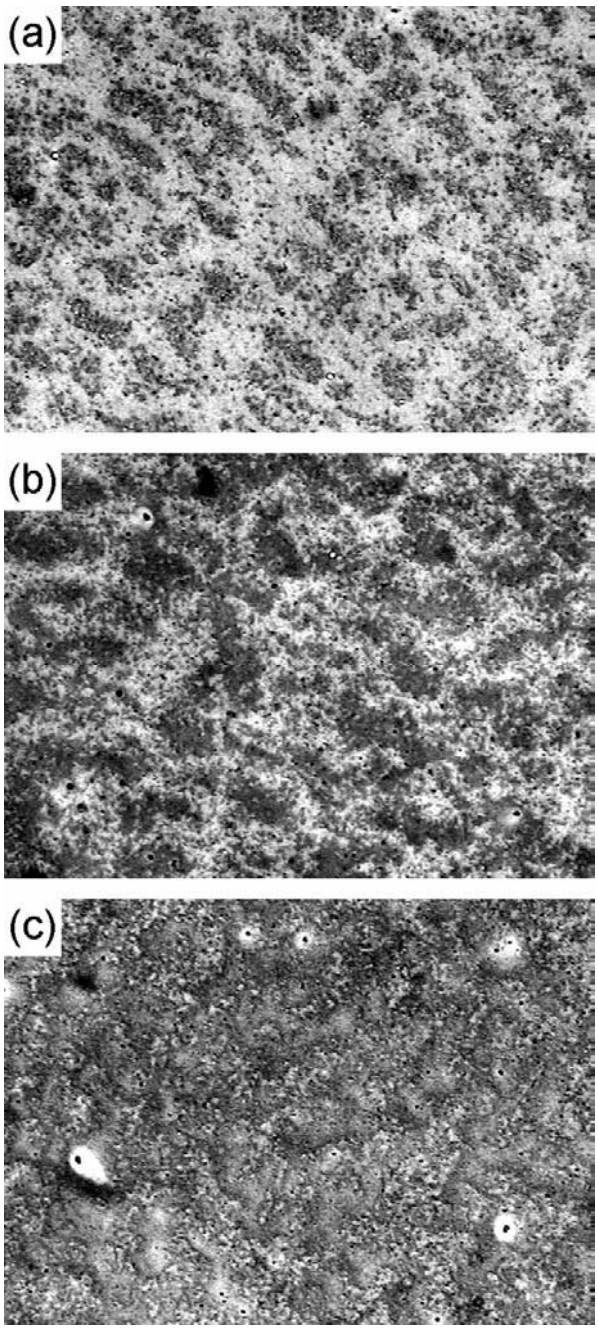

Figure 3.7: 650μm×900μm OM images (reflection mode) of PS + Type-A nanoparticle films, containing: (a) 30.56 mass % particle, (b) 40.00 mass % particle, and (c) 50.00 mass % particle. PS concentration of the solutions is 10 mg/ml for all three films.

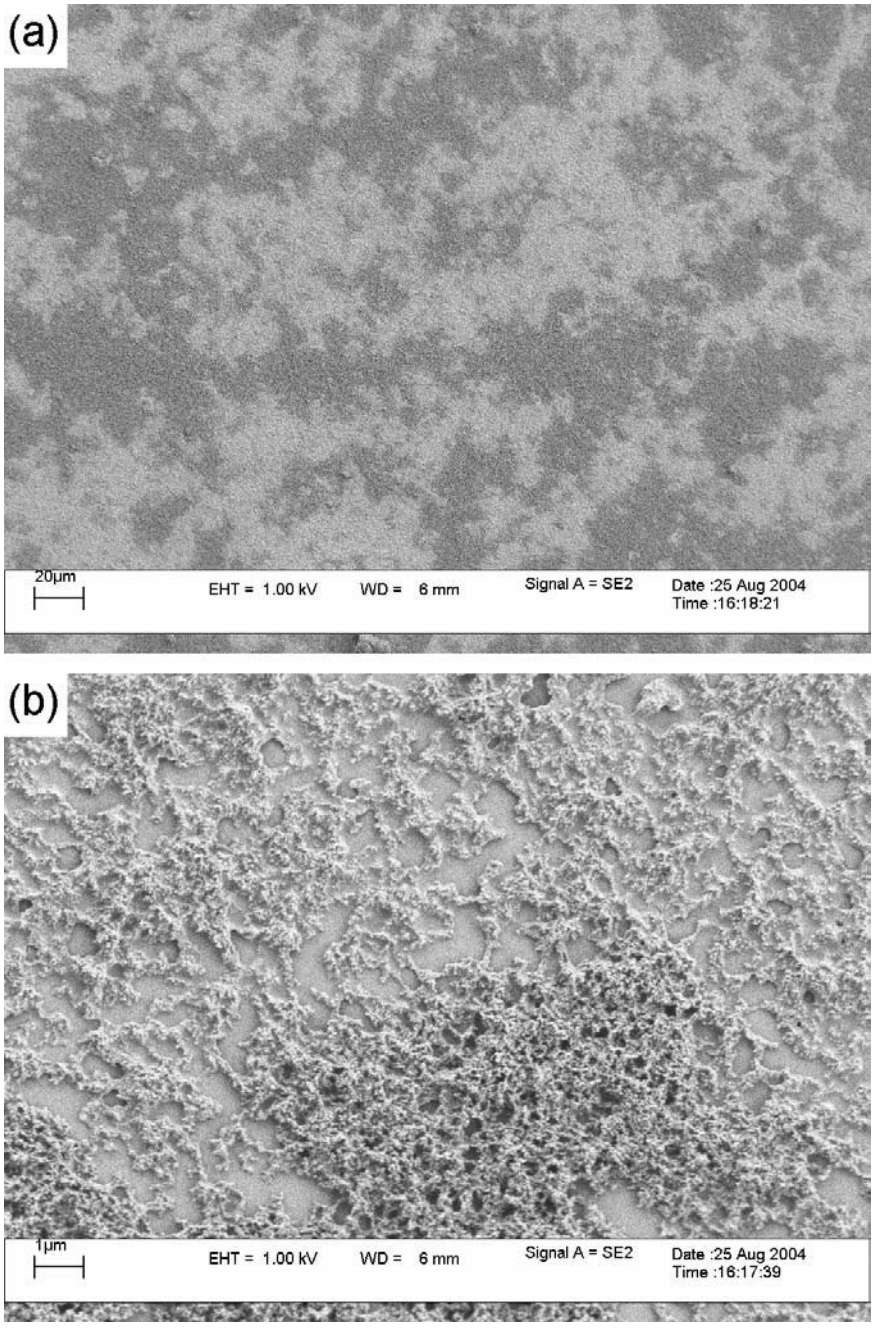

Figure 3.8: SEM images of PS + Type-A nanoparticle film surface obtained from solution having 40 mass % particle with 10 mg/ml PS concentration: a) 265µm×350µm, b) 13µm×17µm.

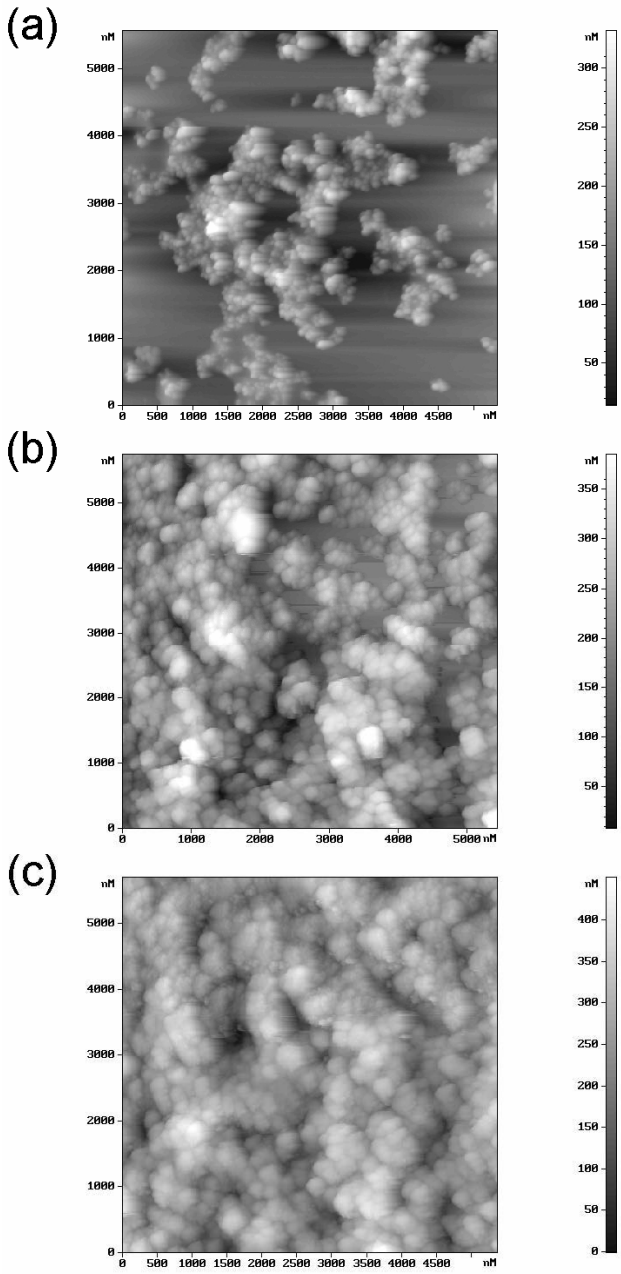

Figure 3.9: 5μm×5μm AFM height images of PS + Type-A nanoparticle films, containing: (a) 48.11 mass % particles (point A in Figure 3.5), (b) 54.40 mass % particles (point B in Figure 3.5), and (c) 69.4 mass % particle (point C in Figure 3.5). Films were prepared from solutions having 5 mg/ml PS concentration.

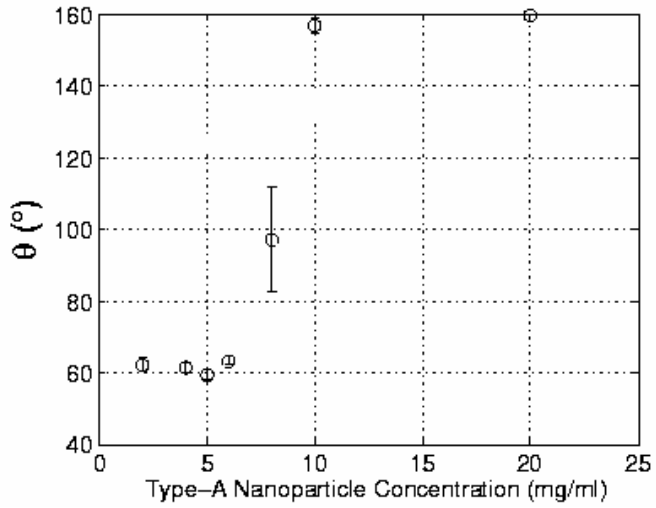

Figure 3.10: Change of contact angle with the concentration of spin-coated solution for films of pure Type-A nanoparticles ($\theta_{substrate}$ = 60°, $\theta_{nanoparticle}$ = 160°).

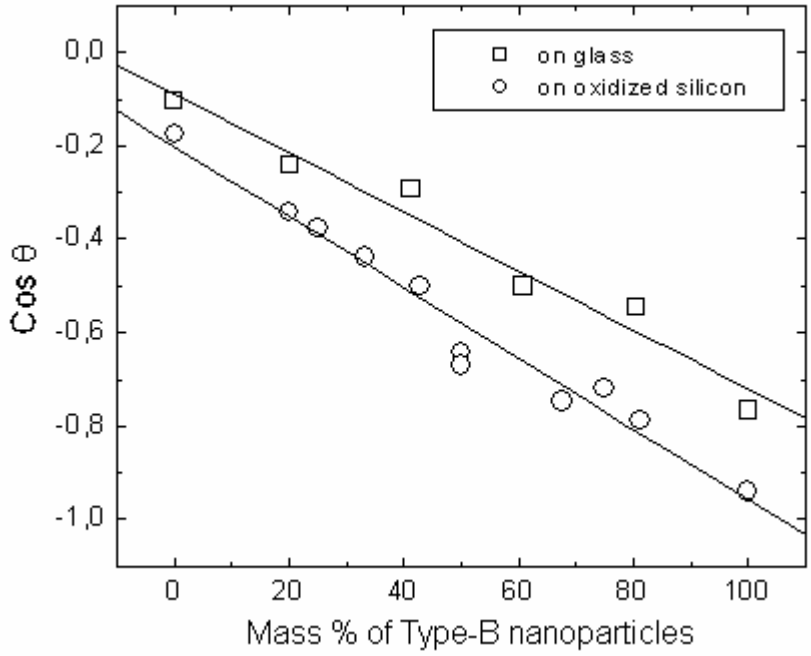

Figure 3.11: Linear change of cosθ with mass % of Type-B nanoparticles on two different types of substrates: glass and silicon. The concentration of PS in the solution was 20 mg/ml.

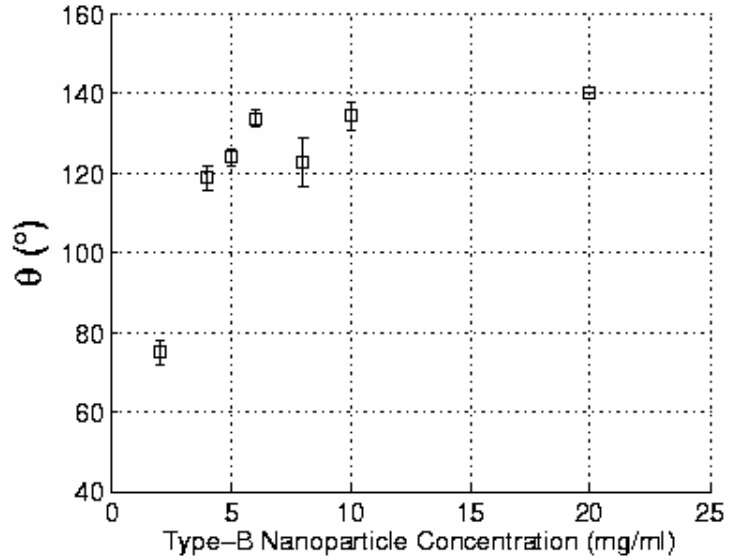

Figure 3.12: Change of contact angle with the concentration of spin-coated solution for films of pure Type-B nanoparticles ($\theta_{substrate} = 60°$, $\theta_{nanoparticle} = 140°$).

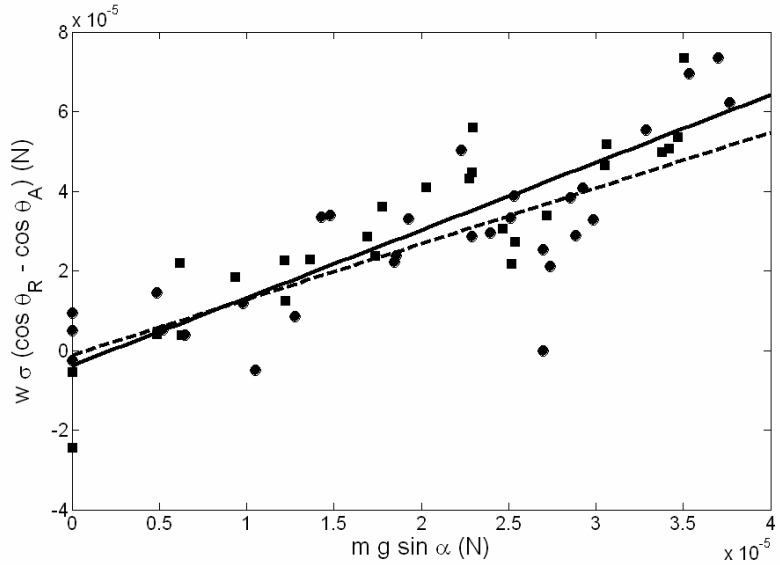

Figure 3.13: Linaer change of pinning force with the gravitational force for PS + Type-A (squares) and PS + Type-B (circles) nanoparticles. The data are collected from films having 10, 30 and 50 mass % nanoparticles (C_{PS} = 10mg/ml). Solid and dashed lines are fits to the data of Type-A and Type-B nanoparticles. Their slopes are 1.7 and 1.4 respectively.

Chapter 4

HYDROPHOBIC SURFACES FROM A TRIBLOCK COPOLYMER

4.1 Introduction

Block copolymers are made up of two or more polymer chains (blocks) that are linked covalently. In case of chemical incompatibility of the blocks, despite their strong tendency to segregate, the blocks are kept tied by the covalent bond, resulting in a phase separation with a length scale of the order of tens of nanometers (microphase separation). This is a length scale desired to be achieved in both science and technology. Examples from science are biological studies and quantum electronics [28,29], and from technology hybrid electronic devices and miniaturization of magnetic storage media [30,31]. Phase behavior of block copolymers, their morphologies in thin films, and some potential applications have been comprehensively reviewed in literature [32-35].

A very promising application area of block copolymers is their use as template structures. This possibility interests almost all research and manufacturing below micrometer size such as cell growth [36], semiconductor applications [37], and nanowire fabrication [38]. The same potential is also important for wettability studies. The most efficient strategy of obtaining super-hydrophobic surfaces has been shown – by the inspiration of nature– to generate two levels of roughness: a large one at a scale of ~10μm, and a small one at the submicrometer level superposed onto this [39]. Studies with fractal surfaces [40,41] and galvanic cell corrosion [42] have demonstrated successful examples of this strategy. The unique templating properties of block copolymers can be used in forming the smaller-scale roughness necessary for superhydrophobicity. The first part of the present chapter appraises this possibility.

Specifically, selective delivery of homopolymers and/or nanoparticles on one phase of the copolymer film is considered as a method of gaining organization on the surface.

Self-organized structures can also be obtained from block copolymers in solutions prepared with solvents selective to one of the blocks. Micelles of different length scale may result depending on block sizes, solvent, concentration and many other parameters. Superhydrophobic surfaces have been recently prepared from micellar block copolymer solutions [43,44]. Following the same approach, second part of the chapter concentrates on block copolymer solutions in selective solvents.

The polymer used in this study is a symmetric triblock Poly(ε-caprolactone)–Poly(dimethyl siloxane)–Poly(ε-caprolactone) (PCL–PDMS–PCL) copolymer. PCL is a hydrophilic semi crystalline polymer ($\theta = 60°$, $T_m = 64°C$) and PDMS is a hydrophobic amorphous polymer ($\theta = 110°$, $T_g = -123°C$) [45]. The triblock copolymer is slightly hydrophilic with $\theta = 88°$.

4.2 Experimental

The PCL–PDMS–PCL triblock copolymer (commercial name: "Tegomer H-Si 6440 P") was kindly provided by Degussa Goldschmidt Industrial Specialties. The blocks have weight-averaged molecular weights of 2000-2400-2000 g/mol respectively, as determined by the manufacturer. Melting temperature of the spin-coated films was measured to be 52±1°C by heat stage optical microscopy.

For thin film morphology studies, block copolymer solutions were prepared in THF (tetrahydrofuran) at varying concentrations from 0.5 mg/ml to 20mg/ml, kept in ultrasound at 60-65°C for 20 minutes, and then immediately spin-coated at 2000 rpm for 1 minute using a Specialty Coating Systems Model 6708D spin coater. Silicon wafers ((100) surface), hydroxylized by 20 minutes of UV-O treatment (Jelight Company, Inc. UVO-Cleaner Model 42-220), were used as substrates. Water contact angles of these substrates were measured to be less than 5°. Temperature and relative humidity during coating were within 23-26°C and 39-51% respectively. Solvent evaporation was maintained first in a laminar flow hood for 10 minutes, then in vacuum

oven for 20 minutes at room temperature. PCL (Fluka, M_r~10,000g/mol) and PDMS ($M_w \approx$ 64,000g/mol) homopolymers were used to understand lamellar ordering and control surface patterning. Thickness measurements were carried out with a high precision ellipsometer (Micro Photonics, Inc. EL X-01R). Each sample was measured at least from three different points and their average was taken.

Nonpolar solvents, extensively OMCTS (octamethylcyclotetrasiloxane), were used for selective-solvent studies. Cyclohexane and n-octane were also tried. Solutions were prepared at various concentrations from 0.5mg/ml to 10mg/ml, and kept in ultrasound at 70-75°C (to erase any history of crystallinity of the PCL blocks) for 20 minutes. They were then cooled either slowly at room temperature for ≈5min, or rapidly by immersing into ice bath for 1min. Their appearance was cloudy both at ≈70°C, and at room temperature. Films were prepared by solution casting from cooled solutions before any visible precipitation had occurred. Glass microscope slides were used as substrate. Solvent evaporation was maintained at ambient conditions in a fume hood by waiting for a sufficient time. Particle sizes in solution were determined by dynamic light scattering, DLS, (Malvern Instruments, Zeta Sizer Nano-S). Contact angle measurements were performed using the same setup as described in Chapter 3.

AFM images were taken with an NT-MDT Solver P47 SPM operated in tapping mode, and OM images were taken with a Leica DMLM optical microscope in reflection mode. No image processing was applied except the second order curve subtraction of AFM height images, which has been employed inherently within the AFM software during recording.

4.3 Results and Discussion

4.3.1 Assessment of the Thin Film Morphology as Template

Thin films of block copolymers exhibit different morphologies depending on the properties of the constituent blocks. A lamellar morphology results when the blocks of an AB or ABA type block copolymer are of comparable molecular weights. The

triblock PCL–PDMS–PCL copolymer used in this study was also reported to have lamellar morphology [46,47]. The two possible orientations in the lamellar morphologies are depicted in Figure 4.1 for the case of this copolymer. The low –in fact one of the lowest ever reported– glass transition temperature of PDMS causes the triblock molecules bend freely over their midblocks [48]. This reduces the symmetric ABA architecture to an effective AB architecture. The lamellae can be oriented either parallel (Figure 4.1.a), or normal (Figure 4.1.b) to the substrate, depending on the orientation of the individual molecules. These two cases are also referred to as flat-on and edge-on respectively. If one of the blocks exhibits much stronger preference for the substrate (in this case PCL), molecules orient vertically and form flat-on lamellae. Alternatively, if the blocks' preferences for the substrate are not so different, molecules orient horizontally and form edge-on lamellae.

Flat-on lamellae give rise to a layered structure with the layer thickness equal to the lamellar spacing. These layers are recognized in AFM height images as clearly detectable flat islands/holes. Their phase images however do not show any difference, since each layer is identical. In the case of edge-on lamellae height images this time give no significant contrast, but alternating strips with certain periodicity are observed in the phase images. These strips correspond to the lamellae perpendicular to the substrate, and their periodicity gives the lamellar spacing. In both edge-on and flat-on cases, lamellar spacing can be determined from AFM analysis.

Figure 4.2 shows OM and AFM images of a ≈110 nm thick film, demonstrating the surface morphology at large (450μm×325μm) and relatively small (16μm×16μm) scales. A layered structure can be seen in the OM image, where the dark regions (holes) are the lower layer underneath the light upper one. Layer thickness is measured to be ≈15nm from AFM height images. A representative cross-section is provided in Figure 1b. The layers are however not as flat and the transition from one layer to the next is not as sharp as one would expect in a flat-on morphology. Strip-like features are realized within the layers.

AFM height and phase images of Figure 4.3 depict the structure within the layers at smaller scale (1.2μm×1.2μm). Same morphology was observed for all layers. Film thickness was ≈45nm. Alternating strips are barely seen in the phase image, which are characteristic for edge-on morphology. Their average periodicity is ≈16nm according to both direct lateral measurements and the 1D Fourier analyses of the profiles taken along different lines.

Figures 4.2 and 4.3 provide contradictory results regarding the orientation of the lamellae. While the presence of layers with a well-defined thickness suggests flat on lamellae, the alternating strips in Figure 4.3.b clearly indicate an edge on standing. However the lamellar spacing obtained from both images is the same (15-16nm).

In order to gain a better understanding of the morphology, PDMS homopolymer was mixed with the triblock copolymer in solution to see its effect on the lamellar spacing of the spin coated films. If the homopolymer penetrates into the lamellae forming a single phase with the PDMS block of the copolymer, this would be observed in the AFM images as an increase in the layer thickness or the strip periodicity. After mixing the two in a wide range of PDMS mass percent from 0.2% to 40% it was understood that PDMS homopolymer does not become included in the lamellae, but rather forms a separate layer at the top of the film. When the low surface energy of PDMS is considered, this result is not surprising. Another possibility for it may be the presence of interlamellar links formed by copolymer molecules that are not bent and have their two PCL blocks in different layers/strips [48]. In this case, incorporation of homopolymer PDMS into the lamellae could have been prevented by these linking molecules for they could not stretch further. The same approach was also tried with homopolymer PCL, and again no change was observed in the lamellar spacing. With a similar explanation, this is attributed to the strong preference of homopolymer PCL for the substrate. It formed a wetting layer between the copolymer film and the substrate.

As an alternative method for surface structuring, homopolymer PDMS solutions were prepared in cyclohexane (nonsolvent for PCL) and spin coated onto block copolymer films obtained in the regular way. For sufficiently dilute solutions, the thin

PDMS layer dewetted in accordance with the periodic stripped pattern of the block copolymer film. This process is interpreted as dewetting and not preferencial adsorption, for it did not happen with relatively concentrated -but still dilute- PDMS solutions. Figure 4.4 shows 1μm×1μm AFM images of the dewetted PDMS, coated from a solution of 0.125mg/ml. The diagonally-extending columnar features are lighter in the height image and darker in the phase image, indicating that they are both higher and more viscoelastic as compared to their surrounding. This suggests that these features are the PDMS regions that have receded and gathered together on the block copolymer surface during dewetting. Height of the PDMS regions was 3-5nm. Water contact angle on these surfaces was measured to be ≈120°.

Figure 4.5 clearly demonstrates that the block copolymer surface acts as a template in the formation of the dewetting pattern. 5μm×5μm AFM height and phase images from the same sample of Figure 4.4 are shown. A grain boundary is seen extending vertically along the image, slightly tilted to the right. The columnar PDMS regions are aligned in different directions on the left and right sides of the boundary and meet at an angle on it. The way they are aligned is not arbitrary, but guided by the morphology of the block copolymer surface.

As with the PDMS homopolymer, hydrophobic nanoparticles (Type-A and Type-B particles of Chp.3) were also tried to be delivered into the PDMS phase of the lamellae both during and after the preparation of the films. Unlike PDMS, resulting nanoparticle distribution on the surface was random. When nanoparticles mixed with PDMS in cyclohexane and coated onto copolymer films, the thin PDMS layer did not dewet.

The difficulty in obtaining successful results with the methods discussed thus far put the lamellar structure of the films into question. Further interpretation of the outcomes of Figures 4.2 and 4.3 requires estimating the sizes of the PCL and PDMS blocks in a single molecule. By straightforward calculations the stretched length of a 2000g/mol PCL chain is found to be 15.49nm. Assuming that the chain is folded once in its crystalline state reduces this value to 7.75nm. Estimating the radius of gyration, R_g, of the amorphous PDMS block by calculations is not very reliable due to high flexibility

of the Si–O bonds. Therefore an empirical relation ($<R^2>_g = 0.274 \times M_w^{0.53}$) was used, and the R_g of a 2400g/mol linear PDMS molecule was obtained as 4.12nm [49]. Based on the possible cases shown in Figure 4.1, these values for PCL and PDMS blocks give a layer thickness or lamellar period of $2 \times 7.75 + 2 \times 4.12 = 23.74$nm. In order to take into account the high compressibility of the PDMS coils, their size are assumed to be the R_g value, rather than $2 \times R_g$. Alternatively the two adjacent PDMS coils can be taken as a single coil of $2400 \times 2 = 4800$g/mol, which gives an R_g of 4.95nm and diameter of $2 \times 4.95 = 9.9$nm. The difference between the two approximations is only $9.9 - 8.24 = 1.66$nm. In either case the calculated and measured values for the lamellar spacing are different.

In addition to this difference, the layered structure in Figure 4.2 and the alternating strips of Figure 4.3 are contradictory observations, if a lamellar morphology is to be accepted. The only structure that can generate both features is a cylindrical morphology similar to the one illustrated in Figure 4.6.a. Layers are formed by cylinders arranged side by side. These cylinders also from a stripped structure within each layer. Their diameter defines both the layer thickness, and the period of the alternating strips.

Two possible molecular organizations that yields cylindrical structures are shown in Figure 4.6.b. In the first possibility PCL block of one molecule clamps with that of the next molecule during crystallization, forming a chain-like PCL line with pendant PDMS blocks. These pendant PDMS blocks can be at any azimuthal position, which causes some of the PCL chain to be exposed from the opposite side. Therefore, when looked at a constant azimuthal angle, the cylinder will have a banded appearance with arbitrary regions of PCL and PDMS blocks. Assuming the size of the PDMS blocks to be $\approx R_g$, diameter of the cylinders is calculated as $7.75 + 2 \times 4.12 = 15.99$nm. This value is in agreement with the experimentally measured layer thickness and strip periodicity. As a second possibility the molecules can organize into two concentric cylinders, with the inner one composed of PCL blocks and the outer one PDMS blocks. This is a more closely packed structure when compared with the first one, and will have a uniform appearance when looked outside. Again assuming the size of the PDMS blocks as $\approx R_g$

cylinder diameter becomes 2×(7.75 + 4.12) = 23.74nm, which is not consistent with the measured layer thickness or strip periodicity of 15±1nm. In addition to this inconsistent diameter, the second possibility is also ruled out by the contact angle measurements. According to this model the cylinders are all covered with the PDMS blocks, and hence contact angle of the films are expected to be close to that of PDMS. However, as mentioned in Section 4.1, films of the PCL–PDMS–PCL block copolymer have water contact angle of $\theta \approx 88°$. This value favors the first possibility; banded cylinders with both blocks exposed will give a contact angle between those of PCL and PDMS.

The cylindrical morphology also explains why the layers are not as smooth, and the height difference between them is not as sharp as it would be for the flat-on lamellar case: Cylinders can cross or twist each other like a knit, resulting in a rougher surface: or they can continue between successive layers, smoothening the height differences between them. Figure 4.7 shows an evidence of the former, and Figure 4.8 of the latter.

4.3.2 Superhydrophobic Films Prepared from Solutions in Selective Solvents

Amphiphilic block copolymers with hydrophobic and hydrophilic segments associate into micelles in selective solvents. These micelles can be of different shapes such as spheres, cylinders or bilayers.

Introducing the PCL–PDMS–PCL block copolymer into a nonpolar solvent is expected to give core-shell structures, wherein the hydrophilic PCL blocks will organize to form the core region and the hydrophobic PDMS shell will shield the core from nonpolar medium. With the procedure outlined in Section 4.2, the PCL blocks in the core will crystallize as the solutions are cooled (following sonication). This is expected to help micelles maintain their structure, perhaps even if they are put in polar medium (at a temperature less than the T_m of PCL).

As a first attempt three different selective solvents were tried with a copolymer concentration of ≈10mg/ml. When casted into films, only the solutions prepared with OMCTS showed superhydrophobic behavior with water contact angle ≈162±2°, and CAH <5°. Considerable difficulty was experienced in placing the drops on the surface.

Contact angle and CAH values reported here probably correspond to possible regions of minor defects, where the drop was able to settle. Effect of cooling rate after sonication was observed to be unimportant for OMCTS solutions. Films from solutions in cylohexane and n-alkane were slightly hydrophobic ($\theta \approx 95°$) and showed large variations in contact angle, indicating problems with coating the substrate, or improper micelle formation. Table 4.1 compares the chemical structures and some of the physical properties of these solvents.

Figure 4.9 shows DLS data of a 1mg/ml block copolymer solution in OMCTS, taken ≈5 min after cooling (note the logarithmic y-axis). ≈100nm size particles are seen initially. These particles then agglomerate (the increase in size until 100th sec.) and sterically stabilize at two different sizes. The larger particle size is ≈2.5μm, whereas the smaller one is ≈300nm. This binary particle size at micro- and nanometer scales is

Solvent	Structure	Boiling Point (°C)	Dynamic Viscosity at 25°C (cP)	Density at 25°C (g/cm^3)
OMCTS	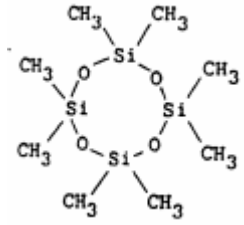	175[50]	2.238[51]	0.9503[51]
Cyclohexane	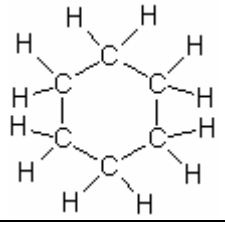	80-81[50]	0.883[52]	0.7740[52]
n-octane	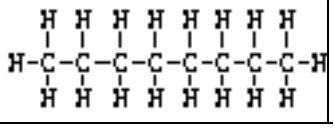	125-126[50]	0.652[52]	0.6989[52]

Table 4.1: Chemical structures, boiling points, dynamic viscosities (at 25°C) and densities (at 25°C) for OMCTS, cyclohexane and n-octane.

precisely what is needed to obtain super-hydrophobic surfaces. Moreover, the sizes are preserved within the measurement time, which is sufficient for film preparation.

AFM investigation of films solution-cast from dilute (0.05mg/ml to 2mg/ml) copolymer solutions in OMCTS confirmed the DLS result. Figure 4.10 presents two 5μm×5μm height images demonstrating the ≈2.5μm-size and ≈300nm-size particles observed in DLS. The ≈2.5μm-size particles correspond to large cylindrical micelles, whereas ≈300nm-size particles to the round spherical micelles. Same structures were also observed with OM.

Two approaches were tried to control the particle size, which in turn is anticipated to yield tunable hydrophobicity. The first approach was to use temperature as a control parameter. DLS scans performed at varying temperatures revealed existence of a strong relation between particle size and temperature. Obtained size versus temperature graph is given in Figure 4.11. As expected, increasing temperature is accompanied by smaller micellar structures. The casting temperature of the films can hence be utilized in adjusting hydrophobicity of the films.

The second approach involved mixing homopolymer PCL with the triblock copolymer. Homopolymer PCL molecules were expected to get included in the core of the block copolymer micelles, which would allow control of the particle size through their relative amounts. DLS analyses however showed that homopolymer PCL molecules did not form integrated structures with the copolymer molecules and remained as undissolved aggregates.

4.4 Conclusion

Self assembly property of block copolymers has been utilized to form patterned hydrophobic surfaces. In the first section the PCL–PDMS–PCL triblock copolymer surfaces were used as a template. Coating block copolymer films with a thin layer of homopolymer PDMS resulted in periodical columnar PDMS regions. These periodic regions were shown to imitate the stripped pattern of the underlying block copolymer surface.

A better understanding of the thin film morphology of the block copolymer has achieved. Layered structure and alternating strips, being characteristics of horizontally and vertically standing lamellae respectively, are observed together in the thin films of the block copolymer. Since lamellae cannot orient horizontally and vertically at the same time, a different structuring composed of cylindrical crystallites has been suggested.

In the second section micellar solutions of the same PCL–PDMS–PCL block copolymer in a nonpolar solvent were shown to contain both micro- and nanometer sized particles. Solution-casted films had water contact angle ≈162±2° and CAH <5°, making them super-hydrophobic. Casting temperature of the films has been suggested as a control mechanism to adjust their hydrophobicity.

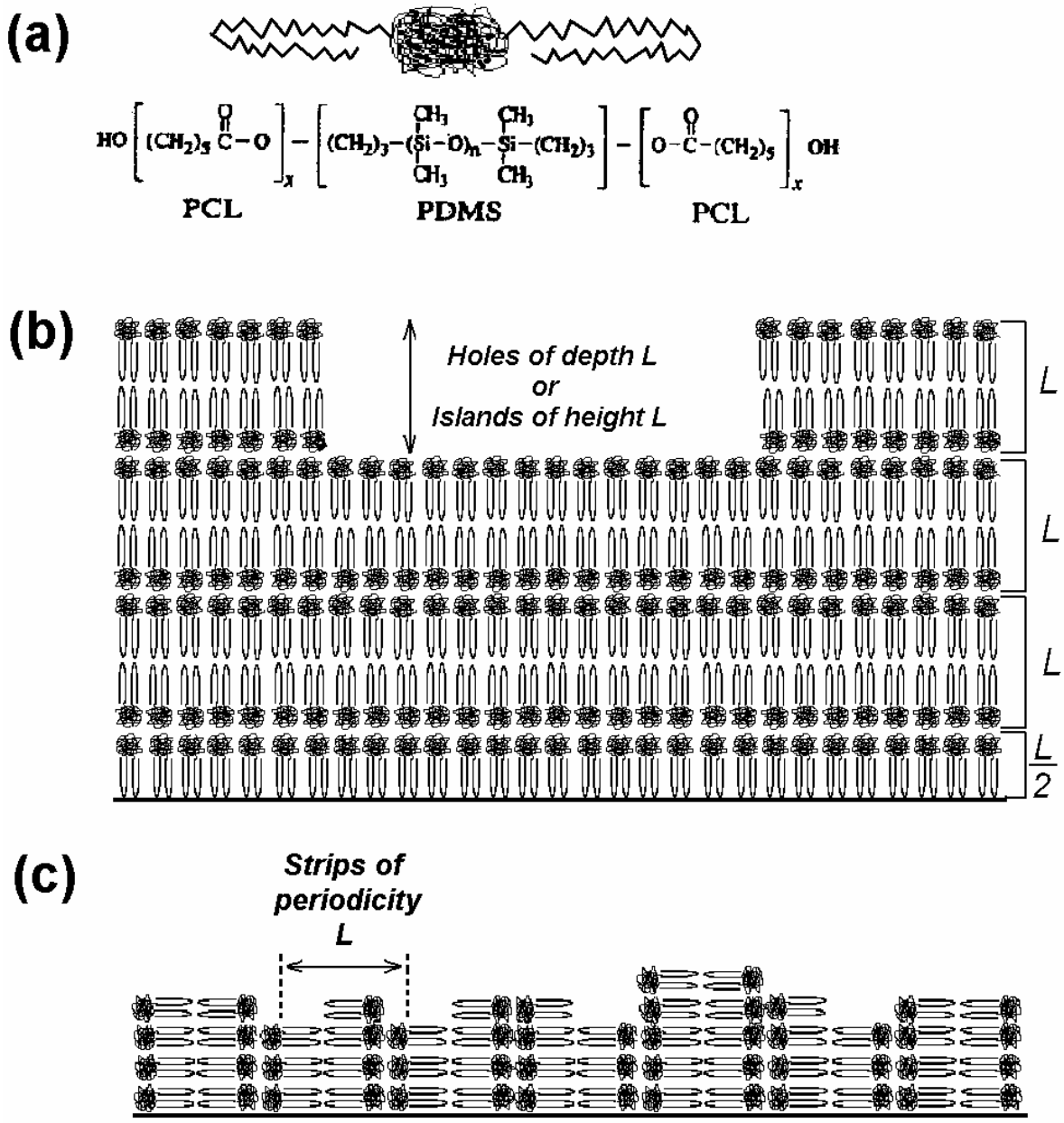

Figure 4.1: (a) Chemical structure of the PCL–PDMS–PCL block copolymer with the blocks matched to the corresponding representation used in the illustrations. (b) Orientations of the molecules (perpendicular to the substrate) and the lamellae (parallel to the substrate) in the flat-on morphology. Layers are formed. (c) Orientations of the molecules (parallel to the substrate) and the lamellae (perpendicular to the substrate) in the edge-on morphology. Strips are formed.

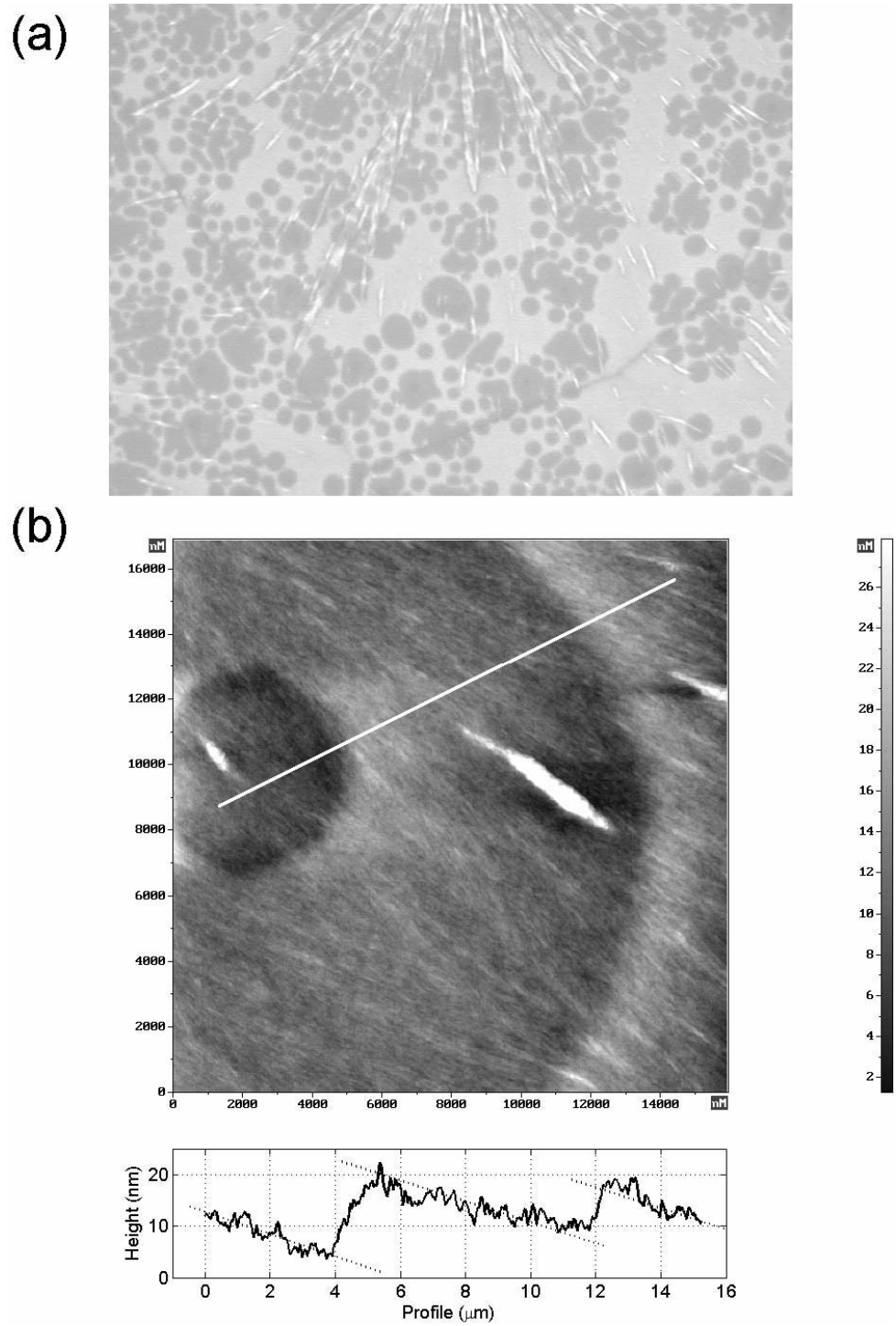

Figure 4.2: 450μm×325μm OM (a) and 16μm×16μm AFM height (b) images of a ≈110nm-thick film. Layer thickness is measured to be ≈15nm from the profile (left to right) taken along the white line in (b). Dotted lines are to guide the eye.

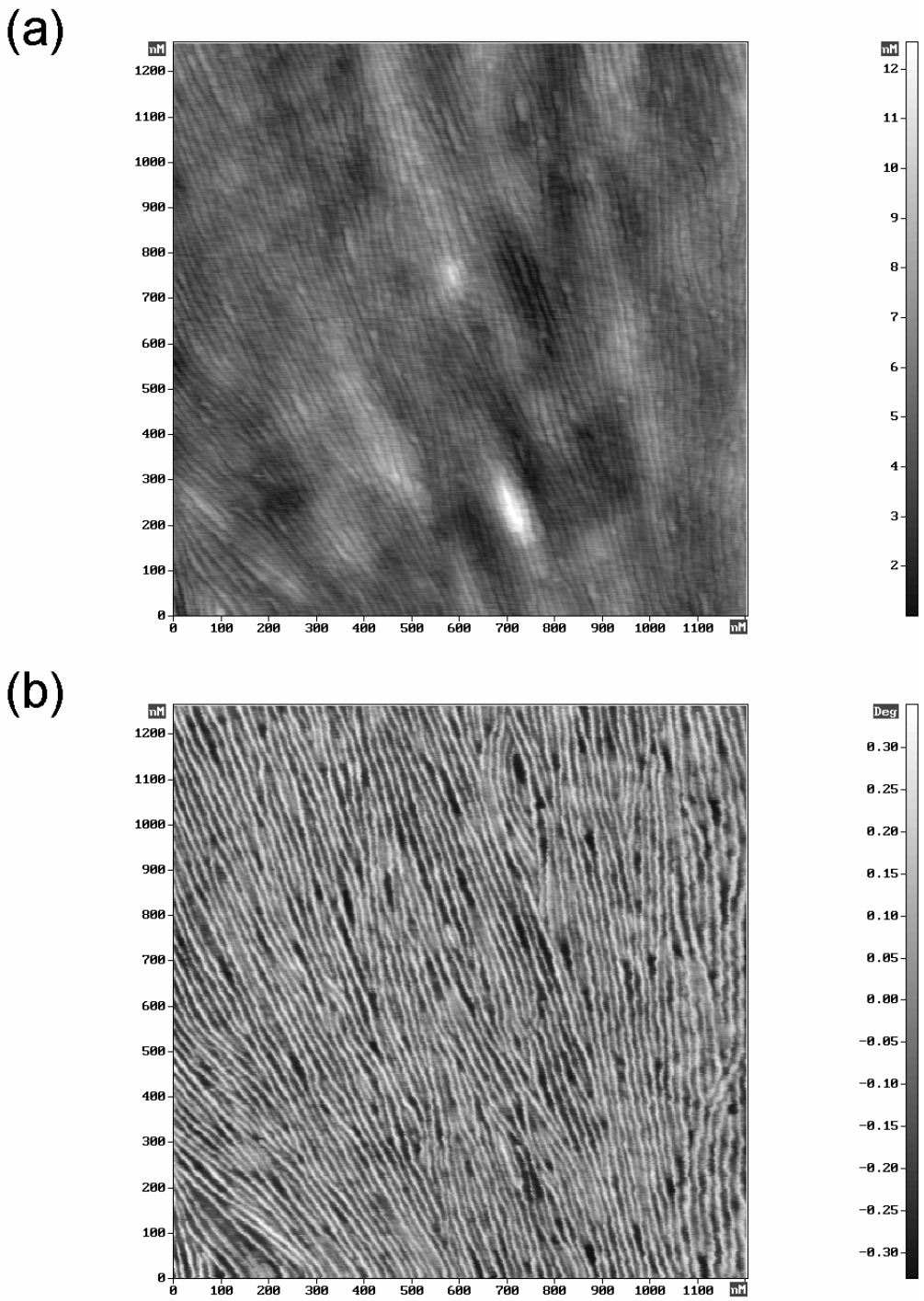

Figure 4.3: 1.2µm×1.2µm AFM (a) height and (b) phase images of a ≈45nm-thick film, demonstrating the structure within the layers similar to the ones shown in Figure 4.2.b.

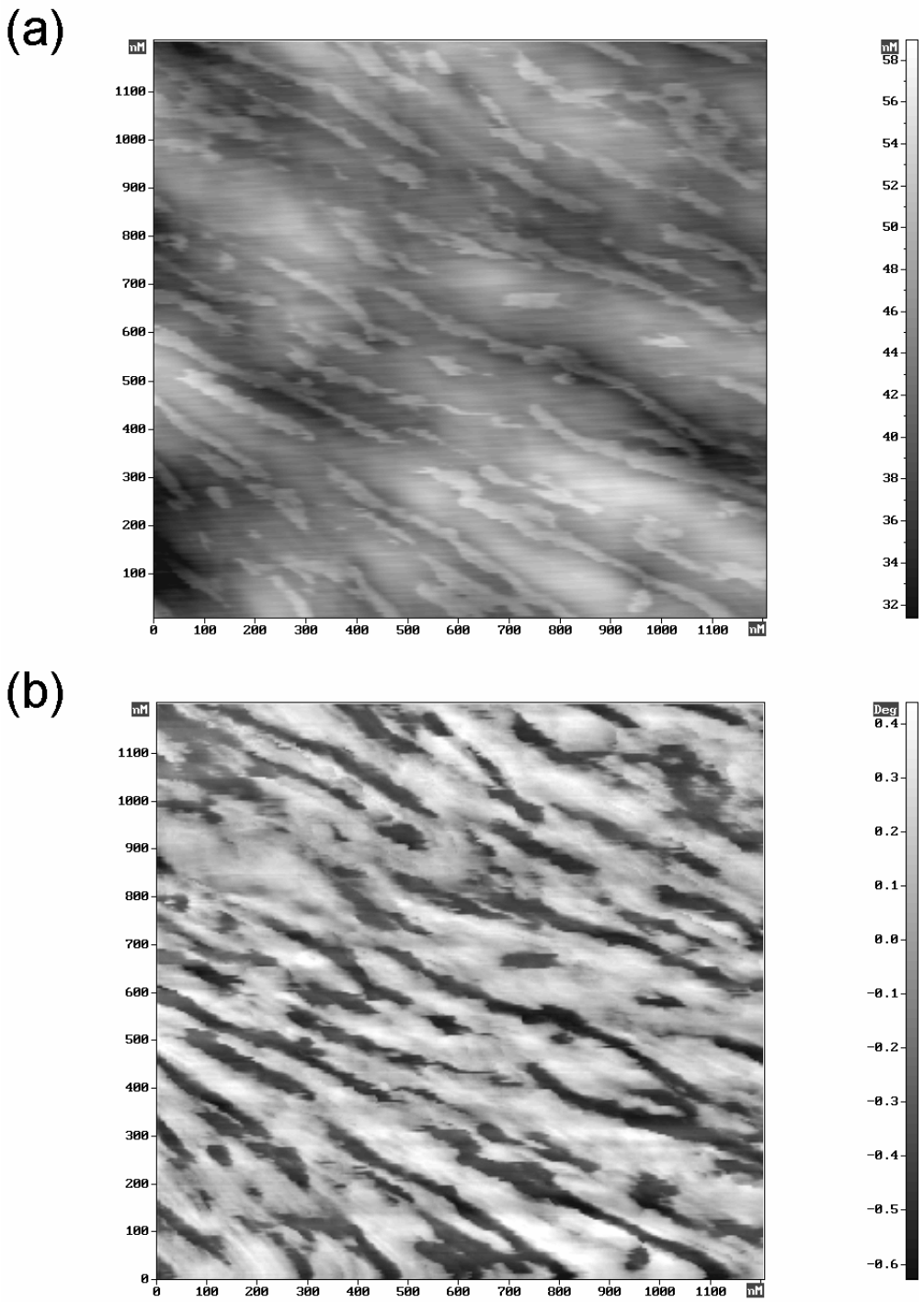

Figure 4.4: 1μm×1μm AFM (a) height and (b) phase images of the dewetted PDMS coated from 0.125mg/ml solution in cyclohexane onto a 106.24nm thick copolymer film. Higher columnar regions in the height image correspond to the dark phase in the phase image.

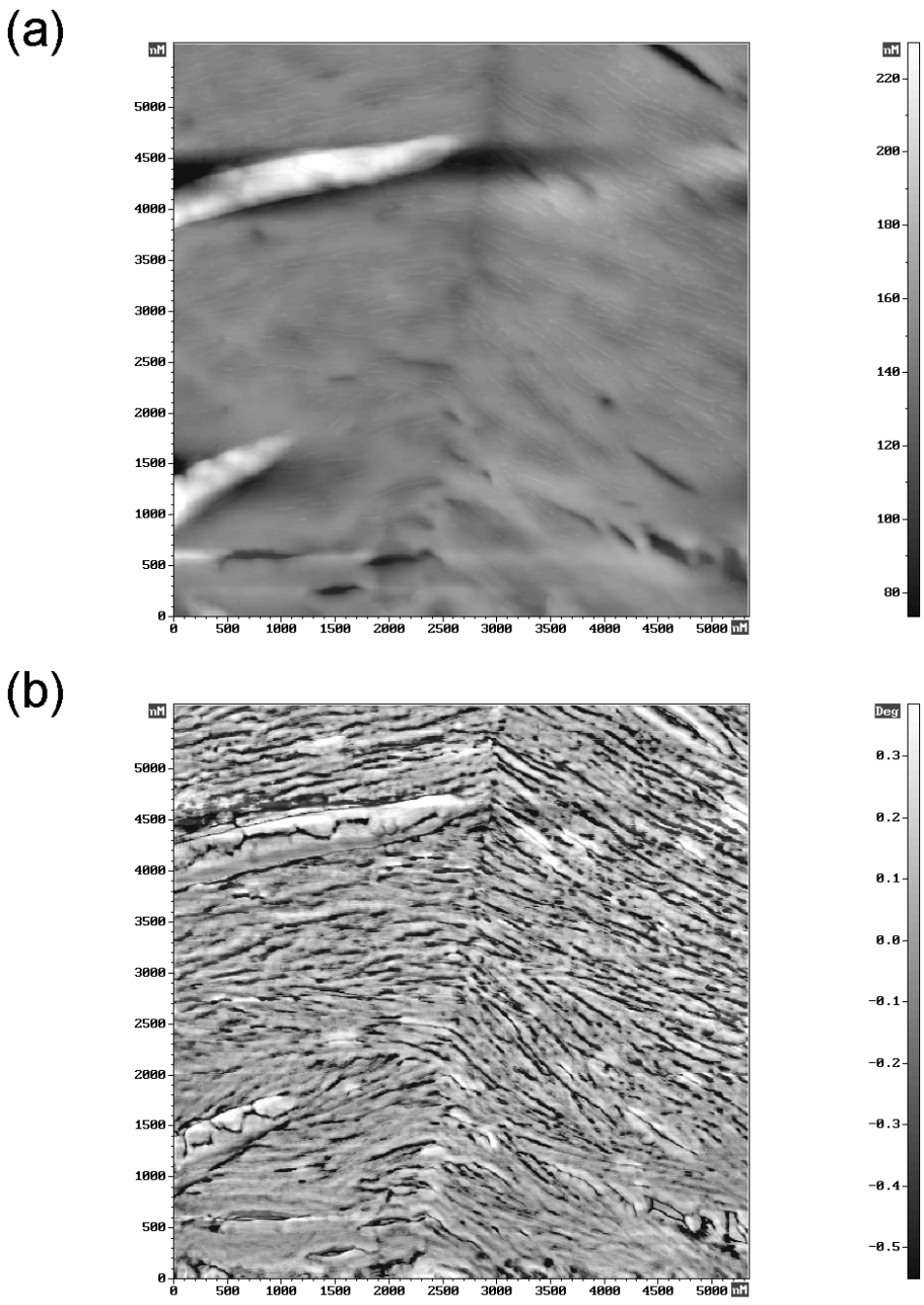

Figure 4.5: 5µm×5µm AFM (a) height and (b) phase images from a 106.24nm thick copolymer film coated with 0.125mg/ml PDMS solution in cyclohexane (the same sample of Figure 4.4). A grain boundary extends vertically along the images. The columnar PDMS regions are aligned in different directions on the left and right sides of the boundary and meet at an angle on it.

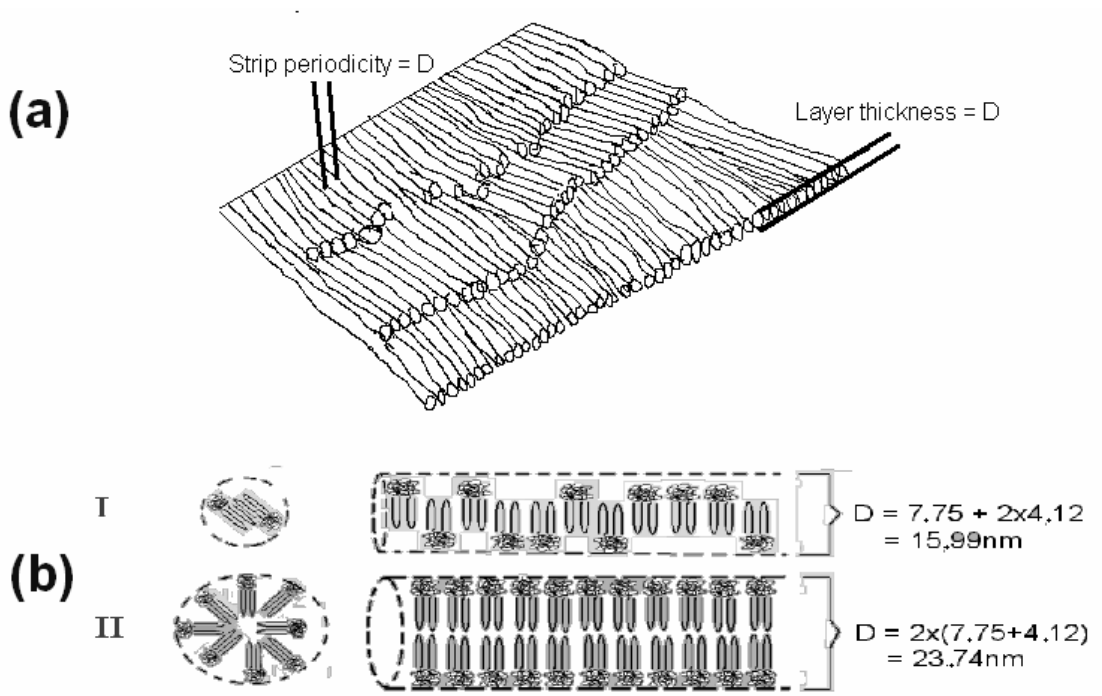

Figure 4.6: (a) Highly schematic illustration of the suggested cylindrical morphology. Thickness of the layers and periodicity of the strips are both equal to the cylinder diameter, D. (b) Two possible scenarios for the formation of cylinders from molecules.

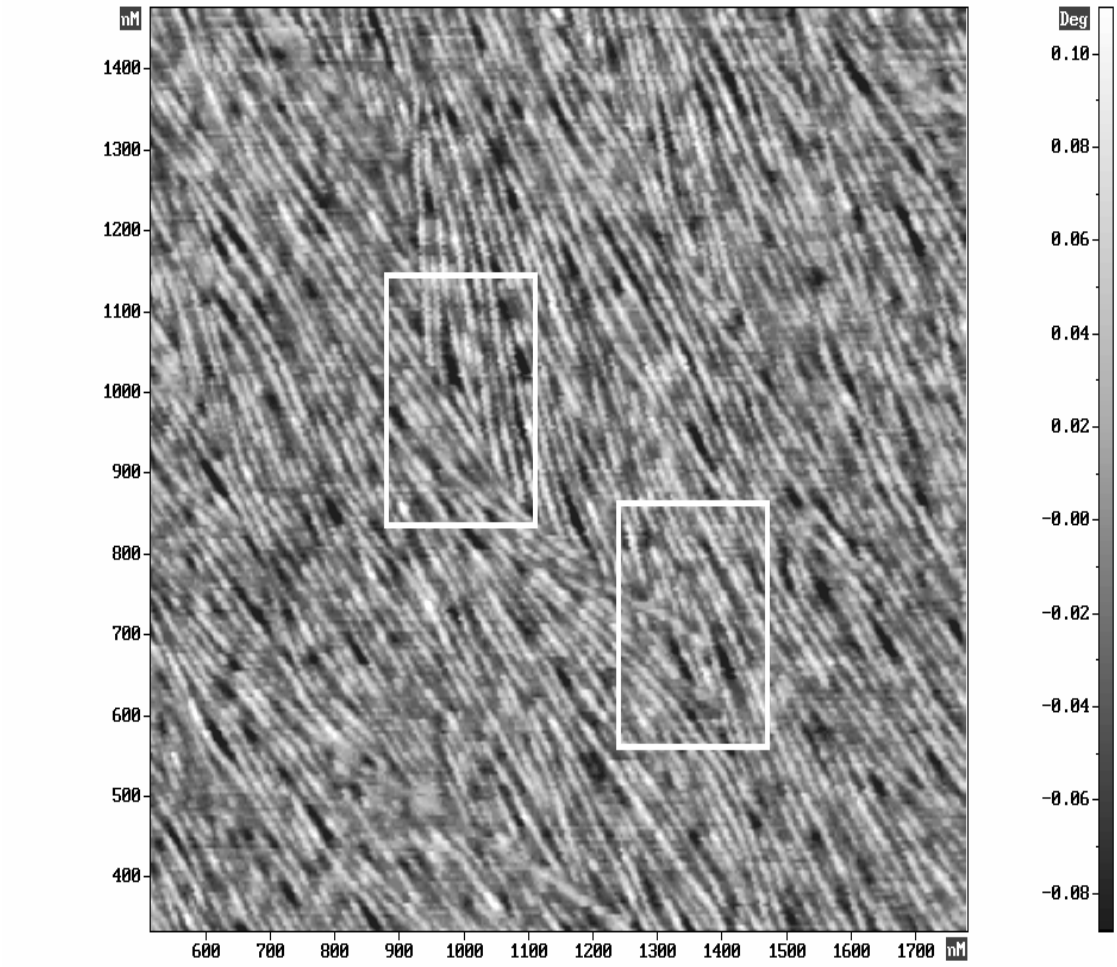

Figure 4.7: 1μm×1μm detail from AFM phase image of the copolymer film showing, in white rectangles, two regions where the cylinders cross each other. Light and dark banded structure of individual cylinders is also seen. These are the exposed PCL and PDMS blocks according to the first model for molecular organization.

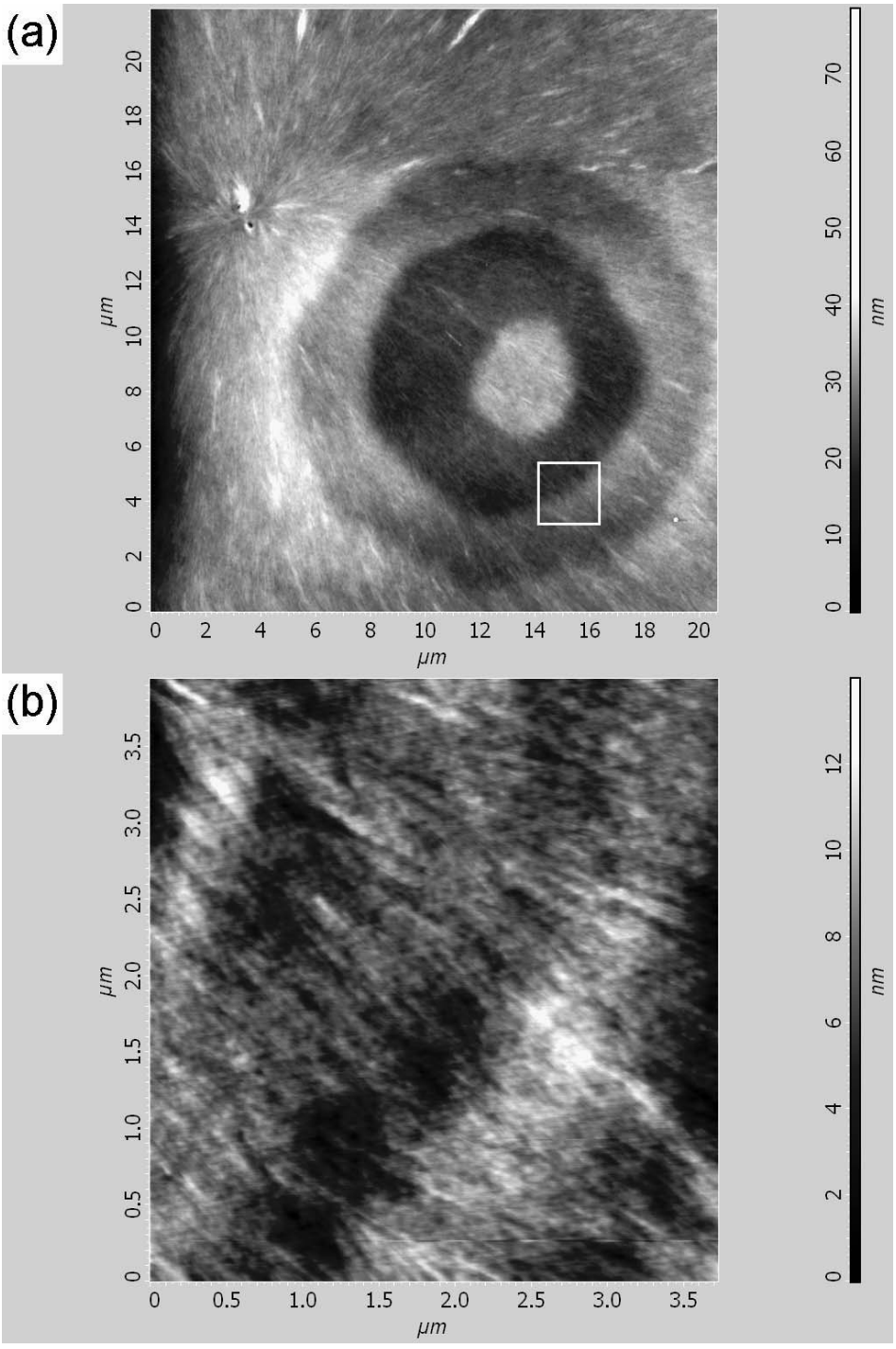

Figure 4.8: (a) 20µm×20µm AFM height image showing three consecutive layers. (b) 3.5µm×3.5µm height image scanned from the layer boundary marked with a rectangle in (a). Individual cylinders extending from one layer to the other are seen.

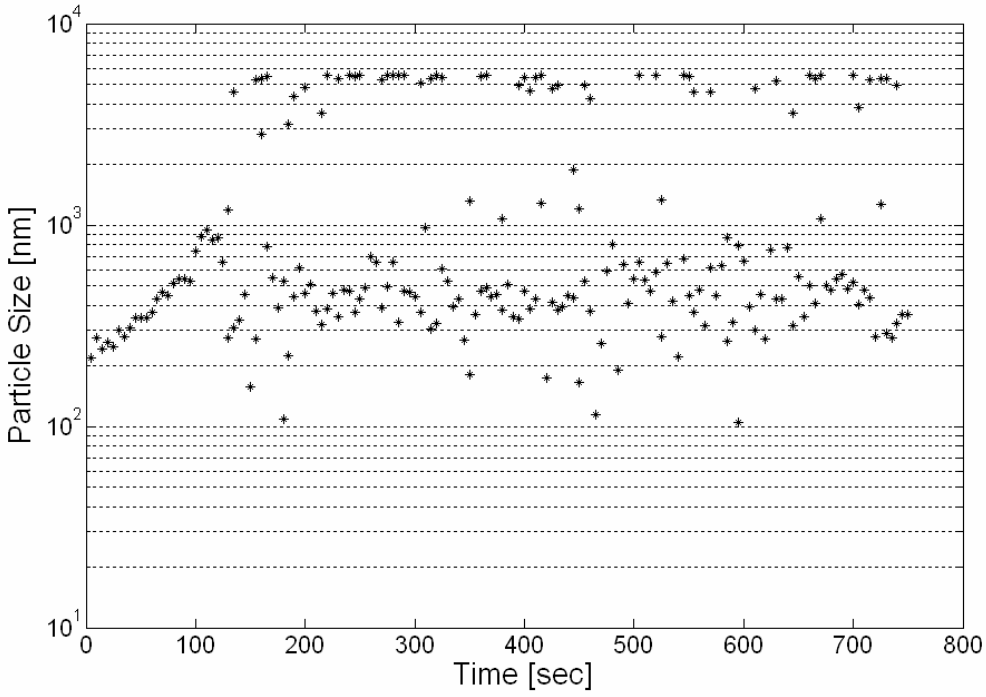

Figure 4.9: DLS data of a 1mg/ml block copolymer solution in OMCTS, taken after ≈5 min after cooling. Particle sizes are plotted in logarithmic axis to emphasize the binary accumulation at micro- and nanoscale.

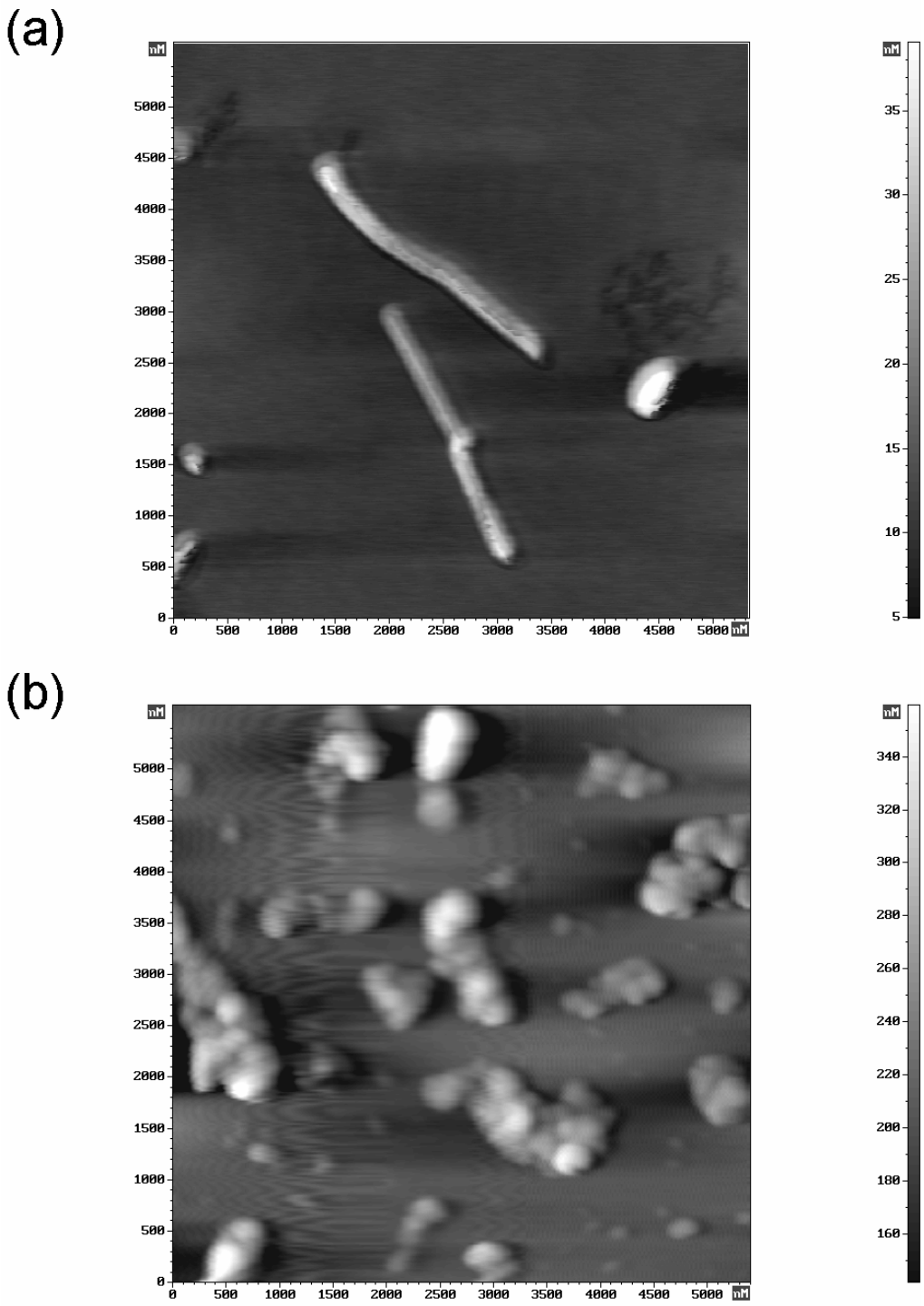

Figure 4.10: 5µm×5µm AFM height images demonstrating the (a) ≈2.5µm-, and (b) ≈300nm-large core-shell particles observed in DLS.

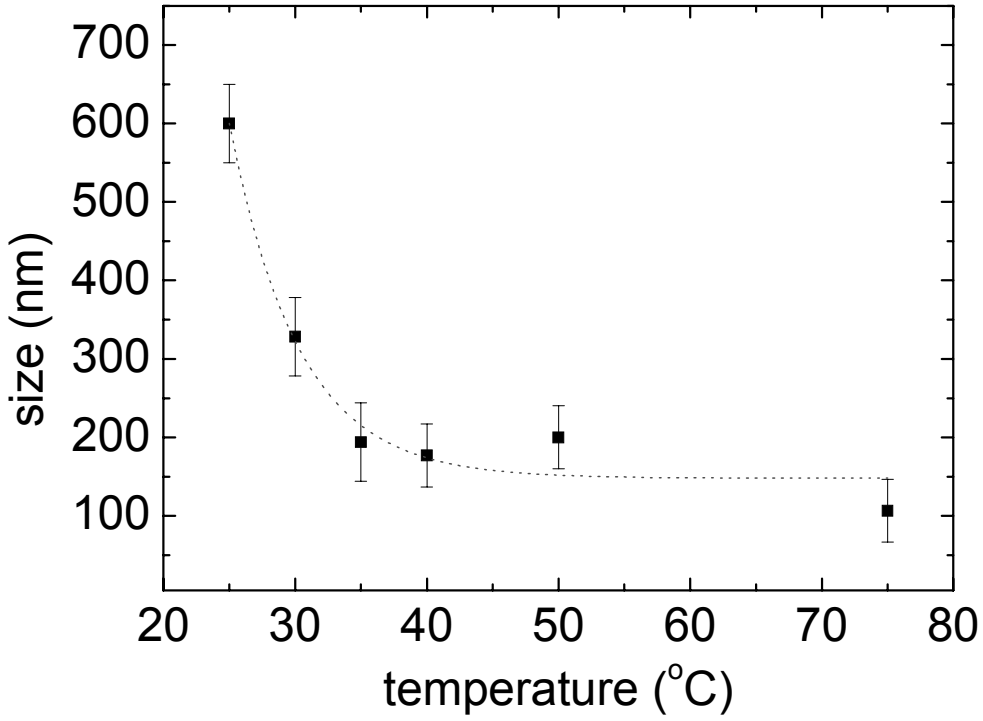

Figure 4.11: Particle size – temperature relation for PCL–PDMS–PCL block copolymer in OMCTS.

Chapter 5

CONCLUSION

In this thesis new methods were sought for preparing, and efficiently characterizing hydrophobic surfaces. Facile methods that would yield tunable hydrophobicity have been developed. CAH has been shown to be an invaluable characterization tool in differentiating between joint effects of various experimental parameters on wettability.

The most important outcome of the efforts in characterization part is the comparative use of contact angle and CAH data that have been gathered as a function of the same experimental parameter. Applying this method in Chapter 2 made it possible to successfully predict -without any single microscopy image- that the sharp change in contact angles observed for Type-A system was due to composition. CAH data has also proven to be a sensitive indicator of the dominant wetting regime (Wenzel or Cassie-Baxter) and any possible transition to the other one. It was also shown that both high roughness and low surface energy (high intrinsic contact angle) are required to have surfaces with static contact angles >120°-130°. However, a very small/high roughness alone is enough to obtain low CAH. The effect of surface chemistry was understood to be significantly smaller on CAH when compared to that of roughness. This suggests that super-hydrtophobicity can also be obtained using heterogenous surfaces.

In the preparation part, the first study involved polymer-nanoparticle composite films. Hydrophobicity of the films could be tuned by composition through nanoparticle amount. As the nanoparticle mass % increased, the surfaces gradually turned from a polymer-rich smooth surface into a nanoparticle-rich rough one. Accessible contact angle range was 93°-160° for Type-A particles and 93°-140° for Type-B particles. The lower range of Type-B particles was compensated by the finer control they provided.

Change of contact angle with particle mass % exhibited a discontinuity in the films of Type-A nanoparticles, whereas the same relation was smooth for Type-B. Dispersion quality of the nanoparticles in the amorphous polymer matrix, being a composition effect, was shown to determine the control sensitivity of the contact angles. Although the films with Type-A and Type-B particles showed different behavior in static contact angles, CAH measurements yielded almost identical result. This was in perfect agreement with Chapter 2; a composition effect, big enough to cause significant changes in the static contact angles, was not noticed at all in CAH measurements.

As the next attempt for preparing tunable hydrophobic surfaces microphase separation of block copolymers was used. The periodic structure of the block copolymer film has shown to serve as a template for nanometer scale roughness formation. Layered and striped morphologies were observed together in the thin films of the block copolymer, which was not possible to explain with the conventional lamellar morphologies. We proposed a different morphology based on cylindrical/fibrillar crystallites. Solutions of the same block copolymer in a selective solvent organized into micro and nanometer sized particles. Having two different size levels has been put into use to form roughness at different length scales by casting these solutions into films. Superhydrophobicity was obtained with a water contact angle of ≈162° and a CAH less than 5°. Particle size in the solution exhibited good dependence on temperature, which can be utilized to adjust the hydrophobicity (through roughness length scale) of the resulting films.

BIBLIOGRAPHY

1. R. E. Johnson, Jr., and R. H. Dettre, in *Contact Angle, Wettability, and Adhesion* (Frederick M. Fowkes, ed.), Adv. Chem. Ser., 43, American Chemical Society, 1964, p. 112.
2. R. E. Johnson, Jr., and R. H. Dettre, J. Phys. Chem., **68**, 1744 (1964).
3. T. Young, Phil. Trans. Roy. Soc. Lond., **95**, 65 (1805).
4. R. E. Johnson, J. Phys. Chem., **63**, 1655 (1959).
5. D. Y. Kwok, and A. W. Neumann, in *Surface Characterization Methods: Priciples, Techniques, and Applications* (Andrew J. Milling, ed.), Marcel Dekker, 1999, p. 37.
6. R. N. Wenzel, Ind. Eng. Chem., **28**, 988 (1936).
7. A. B. D. Cassie, and S. Baxter, Discuss. Faraday Soc., **3**, 16 (1944).
8. C. G. Furmidge, J. Colloid Interface Sci., **17**, 309 (1962).
9. D. C. Tretheway, and C. D. Meinhart, Phys. Fluids, **14**, L9 (2002).
10. Y. X. Zhu, and S. Granick, Phys. Rev. Lett., **88**, 106102 (2002).
11. J. Ou, B. Perot, and J. P. Rothstein, Phys. Fluids, **16**, 4635 (2004).
12. C.-H. Choi, and C.-J. Kim, Phys. Rev. Lett., **96**, 66001 (2006).
13. Y. Zhao, Characterization of Amorphous and Crystalline Rough Surface: Principles and Applications, Academic Press, 2001, p. 33.
14. J. P. Youngblood, and T. J. McCarthy, Macromolecules, **32**, 6800 (1999).
15. M. Grunze, Science, **283**, 41 (1999).
16. G. McHale, N. J. Shirtcliffe, and M. I. Newton, Langmuir, **20**, 10146 (2004).
17. S. M. M. Ramos, and E. Charlaix, Phys. Rev. E, **67**, 031604 (2003).
18. S. Semal, C. Bauthier, M. Vonue, J. J. V. Eynde, R. Gouttebaron, and J. De Coninck, J. Phys. Chem. B, **104**, 6225 (2000).
19. H. Murase, K. Nanishi, H. Kogure, T. Fujibayashi, K. Tamura, and N. Haruta, J. Appl. Polym. Sci., **54**, 2051 (1994).
20. S. Pilotek, and H. K. Schmidt, J. Sol-Gel Sci. Technol., **26**, 789 (2003).

21. A. Heilmann, *Polymer Films with Embedded Metal Nanoparticles*, Springer Series in Materials Science, 52, Springer Verlag, 2002.
22. T. Sugimoto, *Monodispersed Particles*, Elsevier, 2001.
23. M. C. Daniel, and D. Astruc, Chem. Rev., **104**, 293 (2004).
24. M. Geoghegan, and G. Krausch, Prog. Polym. Sci., **28**, 261 (2003).
25. M. K. Chaudhury, and G. M. Whitesides, Science, **256**, 1539 (1992).
26. K. Ichimura, S.-K. Oh, and M. Nakagawa, Science, **288**, 1624 (2000).
27. S.-W. Lee, and P. E.Laibinis, J. Am. Chem. Soc., **122**, 5395 (2000).
28. B. Dubertret, P. Skourides, D. J. Norris, V. Noireaux, A. H. Brivanlou, and A. Libchaber, Science, **298**, 1759 (2002).
29. S. T. Selvan, T. Hayakawa, M. Nogami, and M. Moller, J. Phys. Chem. B, **103**, 7441 (1999).
30. B. D. Terris, and T. Thomson, J. Phys. D, **38**, R199 (2005).
31. W. S.Wu, M. Inbasekaran, M. Hudack, D. Welsh, W. L. Yu, Y. Cheng, C. Wang, S. Kram, M. Tacey, M. Bernius, R. Fletcher, K. Kiszka, S. Munger, and J. O'Brien, Microelectron. J., **35**, 343 (2004).
32. M. J. Fasolka, and A. M. Mayes, Annu. Rev. Mater. Res., **31**, 323 (2001).
33. P. F. Green, and R. Limary, Adv. Colloid Interface Sci., **94**, 53 (2001).
34. I. W. Hamley, Nanotechnology, **14**, R39 (2003).
35. R. A. Segalman, Mat. Sci. Eng. R, **48**, 191 (2005).
36. N. Patel, R. Padera, G. H. W. Sanders, S. M. Cannizzaro, M. C. Davies, R. Langer, C. J. Roberts, S. J. B. Tendler, P. M. Williams, and K. M. Shakesheff, FASEB J., **12**, 1447 (1998).
37. K. W. Guarini, C. T. Black, K. R. Milkove, and R. L. Sandstrom, J. Vac. Sci. Technol. B, **19**, 2784 (2001).
38. T. Thurn-Albrecht, J. Schotter, C. A. Kastle, N. Emley, T. Shibauchi, L. Krusin-Elbaum, K. Guarini, C. T. Black, M.T. Tuominen, and T. P. Russell, Science, **290**, 2126 (2000).
39. W. Barthlott, and C. Neinhuis, Planta, **202**, 1 (1997).

40. T. Onda, S. Shibuichi, N. Satoh, and K. Tsujii, Langmuir, **12**, 2125 (1996).
41. M. Miwa, A. Nakajima, A. Fujishima, K. Hashimoto, and T. Watanabe, Langmuir, **16**, 5754 (2000).
42. X. Wu, and G. Shi, Nanotechnolgoy, **16**, 2056 (2005).
43. Q. Xie, G. Fan, N. Zhao, X. Guo, J. Xu, J. Dong, L. Zhang, Y. Zhang, and C. C. Han, Adv. Mater., **16**, 1830 (2004).
44. J. T. Han, X. Xu, and K. Cho, Langmuir, **21**, 6662 (2005).
45. N. Y. Woodbury, *Physical Properties of Polymers Handbook*, American Institute of Physics Press, 1996.
46. A. J. Lovinger, B. J. Han, F. J. Padden, and P. A. Mirau, J. Polym. Sci. B, **31**, 115, (1993).
47. M. A. Childs, D. D. Matlock, and J. R. Dorgan, Biomacromolecules, **2**, 256 (2001).
48. M. W. Matsen, and R. B. Thompson, J. Chem. Phys., **111**, 7139, (1999).
49. S. Gagliardi, V. Arrighi, A. Dagger, and A. J. Semlyen, Appl. Phys. A, **74**, S469 (2002).
50. Fluka Catalog, 1995/96.
51. M. P.-Tulinska, and P. Oracz, J. Chem. Eng. Data, **50**, 1711 (2005).
52. T. M. Aminabhavi, V. B. Patil, M. I. Aralaguppi, and H. T. S. Phayde, J. Chem. Eng. Data, **41**, 521 (1996).